2017

Computational investigation of effects of crosswinds on detailed locomotive geometry with rotating wheels and moving ground plane

Ryan Christopher Zehr
Iowa State University

Computational investigation of effects of crosswinds on detailed locomotive geometry with rotating wheels and moving ground plane

by

Ryan Christopher Zehr

A thesis submitted to the graduate faculty

in partial fulfillment of the requirements for the degree of

MASTER OF SCIENCE

Major: Aerospace Engineering

Program of Study Committee:

Leifur Leifsson, Co-Major Professor
Richard Wlezien, Co-Major Professor
Thomas Gielda
Peng Wei

The student author, whose presentation of the scholarship herein was approved by the program of study committee, is solely responsible for the content of this thesis. The Graduate College will ensure this thesis is globally accessible and will not permit alterations after a degree is conferred.

Iowa State University

Ames, Iowa

2017

TABLE OF CONTENTS

Page

LIST OF FIGURES

Page

LIST OF TABLES

Page

NOMENCLATURE

Symbols

A	Mass-related empirical coefficient of mechanical resistance [N] Frontal area [FT^2]
B	Viscous mass-related coefficient of mechanical resistance [N Sec/FT]
C	Coefficient of aerodynamic resistance [N]
C_{D_U}	Coefficient of drag nondimensionalized by velocity in the x direction [none]
C_D	Coefficient of drag nondimensionalized by total velocity [none]
C_L	Coefficient of lift [none]
C_{SF}	Coefficient of side force [none]
U_X	Velocity parallel to the rails [MPH]
U_∞	Freestream velocity [MPH]
U_Y	Velocity perpendicular to the rails [MPH]
U	Magnitude of Velocity [MPH]
W/T	Wind Speed/Train Speed [none]
ρ	Density [$slugs/ft^3$]
β	Wind Direction Angle [deg]
θ	Crosswind Angle [deg]
y^+	Nondimensional wall distance [none]

Abbreviations

AAR	Association of American Railroads

ABL	Atmospheric Boundary Layer
CFD	Computational Fluid Dynamics
DNS	Direct Numerical Simulation
HST	High Speed Train
MG&RW	Moving Ground plane and Rotating Wheels
SAE	Society of Automotive Engineers
URANS	Unsteady Reynolds-Averaged Navier-Stokes

ACKNOWLEDGMENTS

I would like to thank my committee chair, Dr. Leifur, my co-chair, Dr. Wlezien, and my committee members, Dr. Gielda, and Dr. Wei for their guidance and support throughout the course of this research. I would also like to thank my officemates for putting up with me and help out when I was stuck. My friends for helping me get through this. Thanks to Alex Peters for working with me on trains.

ABSTRACT

Freight trains are used daily to transport goods across the United States. They are a key component in the distribution of items such as coal, cars, and lumber. Trains consume 3.7 billion gallons of diesel fuel in the United States. The fuel consumption is directly related to the wind resistance (or the aerodynamic drag) of the train geometry. Reducing the aerodynamic drag can therefore lead to significant savings in cost and greenhouse gas emissions. This provides great incentive to reduce the aerodynamic resistance of trains. An examination of sources of drag on the complex geometry of a locomotive are presented in this study. Past studies have used simplified bogie (wheel and motor housing) geometries, whereas the current study includes looking at vortical structures in the near field of the locomotive. The investigation used computational fluid dynamics simulation of the unsteady Reynolds-Averaged Navier-Stokes equation with the Menter SST k-ω turbulence model to explore which locomotive components contribute the most to the overall drag. The study used a single wind to train speed ratio of one half and crosswind angles up to 30 degrees. The results were compared to the Davis-Peters equation. The results show that 75% of the total drag is from the front of the locomotive in straight on flow. The percentage of total drag from the front of the locomotive decreased to 40% as the crosswind angle increased to 30 degrees while still being the dominant source. The study also showed an unsteady vortical structure was acting on the locomotive.

CHAPTER 1. INTRODUCTION

1.1. Motivation and Challenges

The current field of train aerodynamics focuses on two problems without linking them: trains going down the tracks without wind, and trains parked on the rails with a normal crosswind. Few simulations have been shared of trains rolling down the tracks with crosswinds up to 30 degrees. Most of the work on trains going down the tracks have been done on high speed trains (HST), for example, bullet trains or maglev trains. Some of this computational analysis has been done without rotating wheels (Asress and Svorcan 2014). Some simulations describing the shape of the slipstream use detached eddy simulation or large eddy simulation (Baker 2014; Flynn et al. 2014).

Crosswind becomes less important as the speed of the train increases because the angle between the total velocity vector and the train velocity vector becomes small. The aerodynamic resistance (drag) is also not a significant source of resistance in the total system until the train reaches approximately 55-60 mph. This is due to the fact the wind resistance grows with the square of speed. Reducing the total resistance is directly proportional to the amount of fuel burnt, and reducing fuel burn in turn reduces cost and carbon emissions. Most freight trains have a shape similar to Figure 1.

Figure 1. Typical freight locomotive (Silvest 2016)

When measuring drag on a train using computational fluid dynamics (CFD) simulations it is important to include a moving ground plane and rotating wheels. Zhang et al. (2016) addressed this issue and found that the measured drag coefficient can be 6.7% different if this is not included. This would also change the behavior of the boundary layer near the ground.

Another issue with how trains have been studied is most of the CFD simulations are done on highly defeatured models, i.e., the bogies have been simplified to a rectangle with cylindrical wheels (Asress and Svorcan 2014; Flynn et al. 2014; Östh and Krajnović 2014). Most simulations use a solid area to represent the bogies, which house the wheels and motors. This area has a lot of open space. This open space causes air to be captured and increases the drag. The field also has focused on the shape of the slipstream and not what the magnitude of the fluid forces are. This really becomes an issue when crosswind is applied to the simulation because the air is now directly impinging on the bogies. If they were open and had some spaces the air would flow into them usually separating and then causing recirculation regions and pulling the body with the flow.

A simplistic analysis of the drag force on the locomotive will allow for determination if there will be a significant reduction in fuel cost from reducing the drag on only the locomotives. Assuming twenty percent of the total fuel cost is from the aerodynamic resistance, and approximating the average train having one-hundred and fifty cars. Assuming only the aerodynamics of the first car are affected by reducing the drag. This is one seven-hundred and fiftieth of the fuel cost. Reducing the drag count by ten to fifteen counts of drag is equivalent to a tenth of one percent to two tenths of one percent drag reduce on the locomotive. Using this result with the fuel savings on the order of one millionth of the total fuel cost. This would also lead to a proportional reduction in CO2 emissions. This shows that the fuel burnt from drag is

not very large compared to the total fuel burn. The inflow plane from the locomotive to the following car may be more important.

1.2. Research Objectives

The research objective of this work is to describe the unsteady flow phenomena that occur around a detailed freight locomotive in a crosswind using CFD simulations. In particular the objective is to study the breakdown how the sources, of drag changes with increasing crosswind angle. Furthermore, the objective is to include a moving ground plane and rotating wheels to increase the realism of the modeling. The total lift, drag, and side force on the locomotive will be presented. Unsteady CFD was used to complete the objectives.

1.3. Thesis Outline

This thesis contains four additional chapters: background, computational fluid dynamics modeling, results, and conclusion. The background chapter contains information on how resistance has been historically determined, how crosswind has been implemented in the past, and how it is implemented in this work. The computational fluid dynamics chapter describe the geometry setup, grid, and the flow model in this study. The results chapter presents the results of the CFD simulations. The thesis concludes with a summary of the work and provides suggestions for the next steps.

CHAPTER 2. BACKGROUND

This chapter describes the nomenclature, briefly explains train aerodynamics, standards, as well as conventional approaches of computing resistance of trains.

2.1. Train Aerodynamic Computational Fluid Dynamics Standards

The Society of Automotive Engineers (SAE) has a standard that covers computational fluid dynamics of heavy vehicles, called SAE J2966 (Committee 2013). In the standard, SAE proceed to layout a template from how the domain should be configured. The standard does state that the length of the domain should be 9 to14 body lengths of the vehicle. This allows for the wake structure to form behind the vehicle. This also allows for the free stream to reunify any non-uniformities.

2.2. Davis-Peters Equation

Many works have proposed ways to determine the resistance of trains. The popular method is the Davis Equation (Rochard and Schmid 2000). The rolling resistance is calculated as

$$R = A + BV + CV^2, \tag{1}$$

where A and B are related to the rolling resistance and intake air for engine performance, C is the coefficient for aerodynamic drag, and V is the velocity of the Train. Terms A, B and C are regression terms taken from experimental data. Peters (1990) proposed a correction to the aerodynamic

$$C_{D_U}(\theta) = C_{D_{U_{\theta=0}}}\left(1 + \frac{|\theta|}{50}\right), \tag{2}$$

forces term for crosswind flows. Where $C_{D_{U_{\theta=0}}}$ is the drag coefficient with no crosswind, θ is the crosswind angle, and C_{D_U} is the drag coefficient nondimensionalized by velocity parallel to the rails.

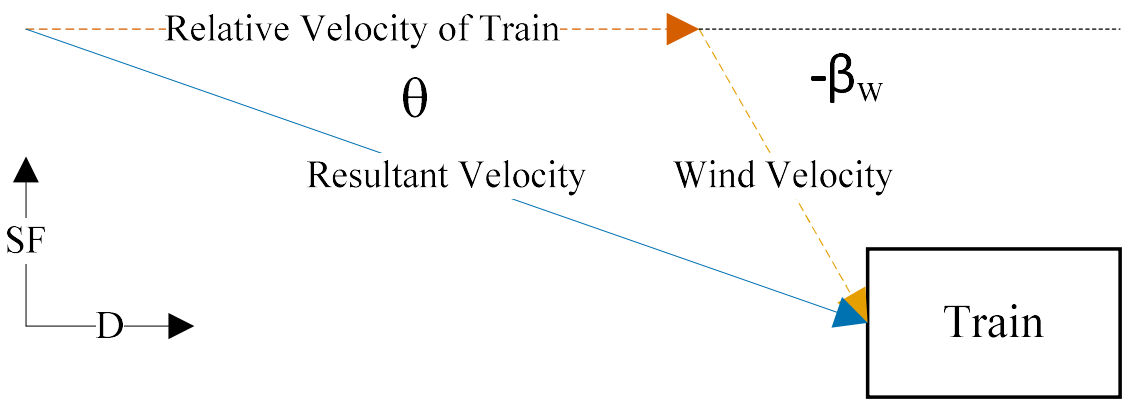

Figure 2. Velocity diagram for train

2.3. Crosswind

When formulating the crosswind portion of the problem the standard formulation of maintaining constant dynamic pressure and rotating the velocity vector was attempted. Figure 2 show the velocity vectors and the angles between the vectors acting on the locomotive and train.

Assuming the train is at constant velocity of 70 mph, rotating the velocity vector requires the velocity of the wind to change. To rotate the vector by thirty degrees (θ) the wind would have to be a speed of 56 mph. This is an extremely fast speed for wind. A better approach would be to specify the wind speed and train speed. Doing this results in dynamic pressure dropping as the wind direction angle (β) increases/decreases. This formulation allows for easier adaptation to non-steady wind.

The relation between wind direction angle and crosswind angle is

$$\theta = \frac{\beta}{|\beta|}\operatorname{acos}\left(\frac{\frac{W}{T}\cos\beta+}{\sqrt{\left(\frac{W}{T}\right)^2+1+2\left(\frac{W}{T}\right)\cos}}\right), \tag{3}$$

The only additional piece of information required to determine θ from β is the ratio of the wind speed to the train speed (W/T). Figure 3 provides a plot of Eqn. (3) for various wind to train

speed ratios. Every ratio has a region where the Davis Peter's equation is valid. Notice that when the wind is pushing the locomotive the width of the validity region is smaller. This means when the wind is pushing a locomotive the coefficient of drag increases, but the dynamic pressure is decreasing. For every crosswind angle, there are two wind direction angles, meaning that the use of the crosswind angle results in an ambiguous formulation of the problem. Figure 4 shows that using the crosswind angle versus velocity magnitude results in a function that fails the vertical line test. There is a unique velocity magnitude for each wind direction

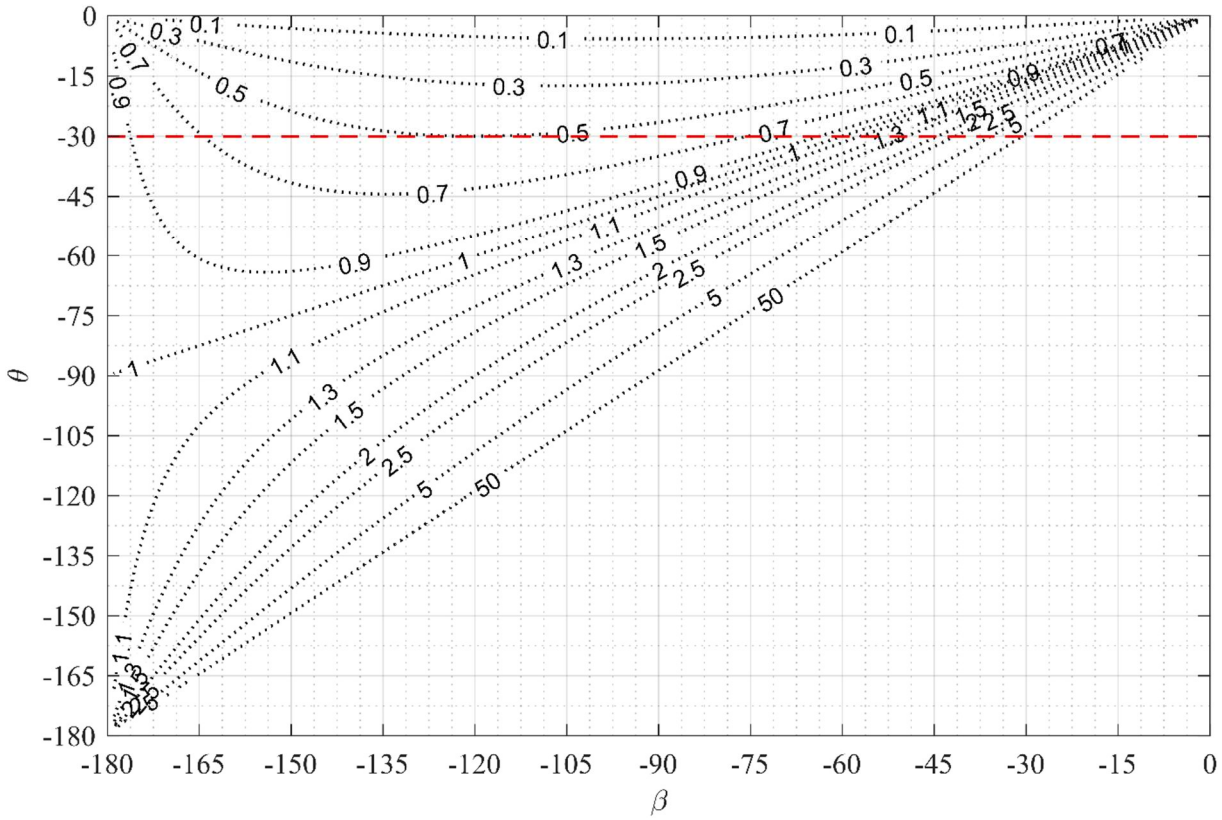

Figure 3. Wind direction angle versus crosswind angle for various wind to train speed ratios

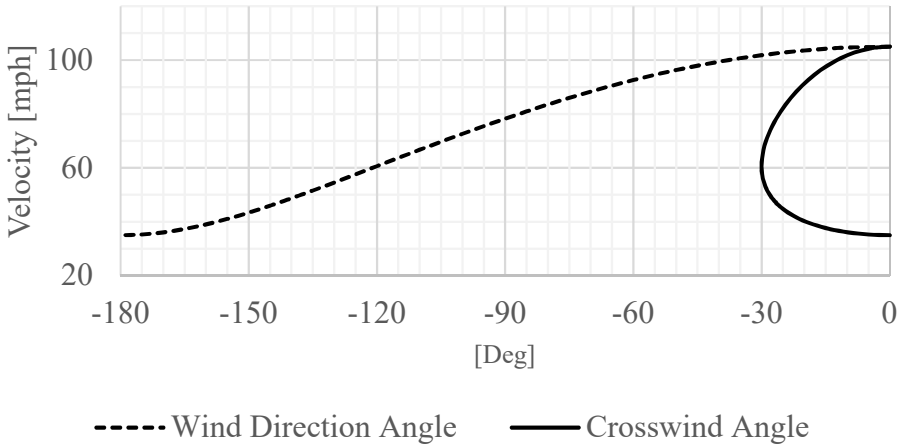

Figure 4. Graph of velocity versus wind direction angle and crosswind angle

2.4. Nondimensionalization

When nondimensionalizing the Davis Peters equation the coefficients use the velocity in the x direction. This makes historic since because the goal was to predict the total rolling resistance down the rails per ton. From an aerodynamics standpoint, when nondimensionalizing a flow the magnitude of the free stream velocity is usually used. If the magnitude of the free stream is not and the wind speed in one direction is used this would lead to misleading results. Where the coefficient appears to be more dependent on the crosswind than it is. In this paper, we will denote two nondimensionalizations. When using only the x component velocity the subsequent coefficient will have a subscript x. The first nondimensionalization

$$C_{D_U} = \frac{D}{\frac{1}{2}\rho U_x^2 A}, \tag{4}$$

where D is the drag force, ρ is the density of air, U_x is the velocity parallel to the rails and A is the frontal area of the train. The second nondimensionalization

$$C_D = \frac{D}{\frac{1}{2}\rho U^2 A}, \tag{5}$$

where U is the total velocity and the rest of the terms are the same as above. The x component coefficient can be determined from the full coefficient by

$$C_{D_U} = \frac{C_D}{\cos^2 \theta}, \tag{6}$$

CHAPTER 3. COMPUTATIONAL FLUID DYNAMICS MODELING

This chapter describes how the CFD was setup and ran. This will include a look at the mesh and the surfaces which were used to extract the data.

3.1. Governing Equations

In this work, the flow past the locomotive is simulated using unsteady Reynolds-averaged Navier-Stoke Equation (URANS) with Menter's SST k-ω turbulence model. The CFD code used for this work was Star-CCM+ version 11.04.010–R8.

3.1.1. The Unsteady Reynolds-Averaged Navier-Stoke Equations

URANS keeps the time averaging terms in the Navier-Stokes equations. This adds to the numerical stability of the system. The same locomotive was initially tested with the steady RANS equations but it had convergence issues and the solution would contain non-physical solutions.

3.1.2. Menter SST k-ω Turbulence Model

The Menter SST k-ω model was chosen for the simulation model as it can handle flows with separation (Menter 1994). However, this turbulence model may over predict separation, which for the present study, may lead to over prediction of separated regions than an actual train.

3.1.3. Implicit Unsteady Coupled Flow Solver

The implicit unsteady solver was used to solve the flow around the locomotive. The implicit solver allows for larger time steps than the explicit solver. There are time step restrictions on the implicit unsteady solver. To determine how large of a time step the simulation could take, two methods were employed. The first method was look at the recommend time step from the Star-CCM+ user manual (CD-adapco 2016). The time step was 1 millisecond. This caused

some stability issues. The second method was to guess and check the time step to see when the solution became stable. The result of this was time step being approximately 679 microseconds.

The implicit unsteady solver uses internal iterations within the time step to converge the flow to the new state. To do this, a parameter was picked to be monitored to verify the inner iterations were converging. The max velocity was monitored and was determined that seven inner iterations per time step allow for the velocity to settle to a constant value.

3.2. Solution Domain

The domain has three distinct areas: the far field, the road bed, the refined wake region. The areas are different due to the size of the phenomena that is occurring in each area. Figure 5 shows an isometric view of the domain. The road bed is finely meshed to ensure the flow around the rails and their influence is captured. The refined wake region is refined to capture the flow before, after, and around the locomotive. This is where the most complex flow phenomena are occurring.

3.2.1. Size and Layout

The overall size of the domain is 200 m x 200 m x 50 m (see Figure 5). The train is located at the center of the domain. The far field has a slip wall where all other walls are non-slip. This was done to control the boundary layer of the ground. Changes to this will be discussed in future work. The locomotive is a represented model of a locomotive with parts borrowed from real trains. The general shape is that of a SD 40. A model was provided by Electric96. In his model, the upper surface was a surfaces body and had too many minute details. By including the minute details the grid would have to grow by a large amount. The top was modeled from a drawing of a SD-40. The result is a locomotive that is 60 feet long.

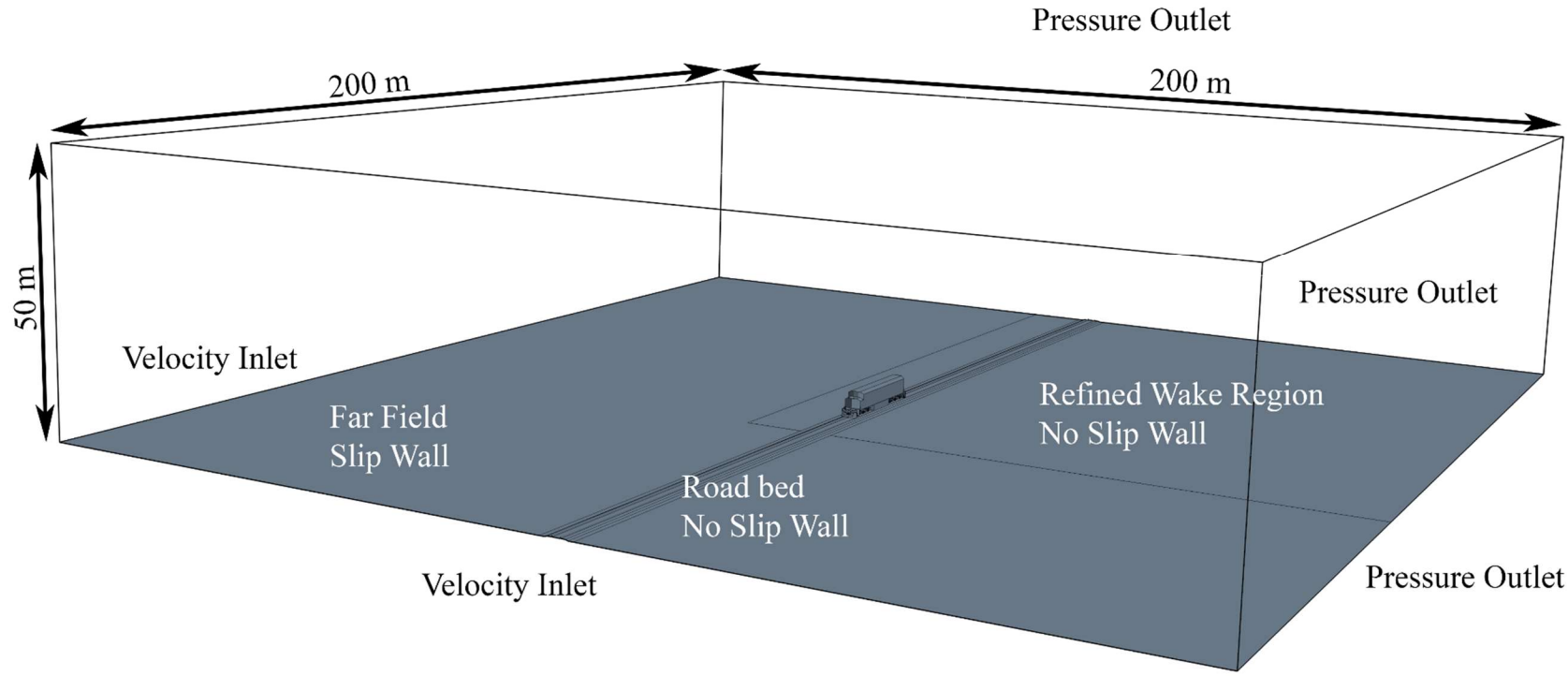

Figure 5 Solution domain overview

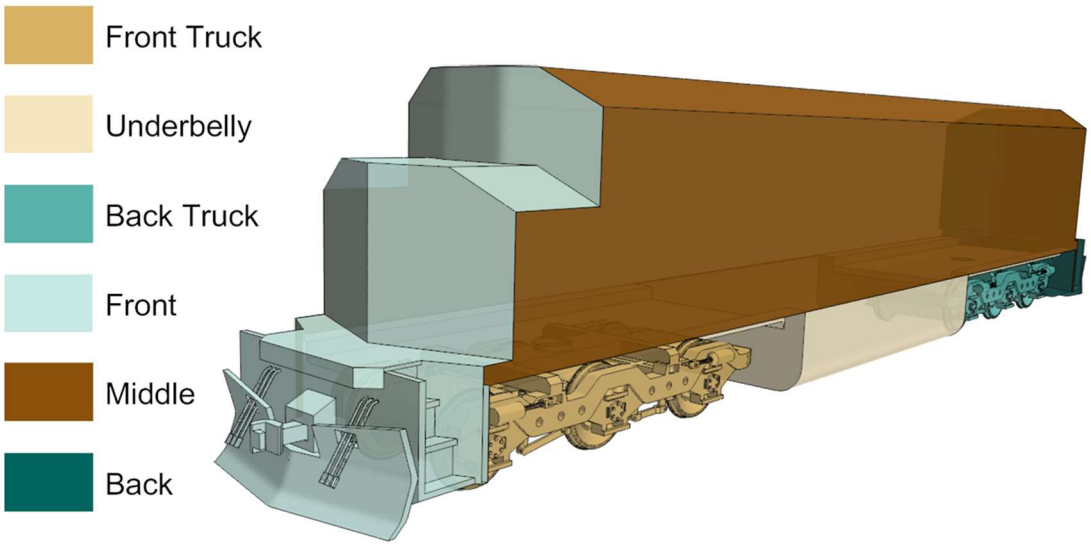

Figure 6. Component breakdown

There are 47 different named surfaces on the locomotive model. These surfaces were grouped into six components. The components are: Front, Back, Middle, Front Bogie, Rear Bogie, and, Undercarriage. These components were chosen because they were simple and intuitive. Figure 6 shows the components that the locomotive was broken down into to bookkeep the drag forces. The back could also be referred to as the base.

3.2.2. Component Breakdown

The upper surface is a simplified SD-40 shape. The doors and sides were simplified. The railings were removed do to the fineness of mess required to discretize and resolve the flow on and around them.

The lower part of the locomotive are bogies for SD-40. The original wheel from his model were removed because they were just cylinders. The couplers were also replaced with AAR standard couplers. The couplers were defeatured by removing some of the minute details but have the same bulk features. Figure 7 shows the front component which consists of the plow, stairs, coupler, hydraulic lines, and the cab. Figure 8 show the middle component which consists of the sides of the locomotive and the roof. Figure 9 shows the back component which

consists of the plow, stairs, coupler, hydraulic lines, and the cab. The front bogie has the frame, engine cases, wheels, suspension, brakes, and brake lines. The complexity of the bogie is still defeatured from a real bogie but will allow better insight than models previously presented in literature. Figure 10 shows the bogies on a real SD-40. Figure 11 show the bogies that were used in the simulations.

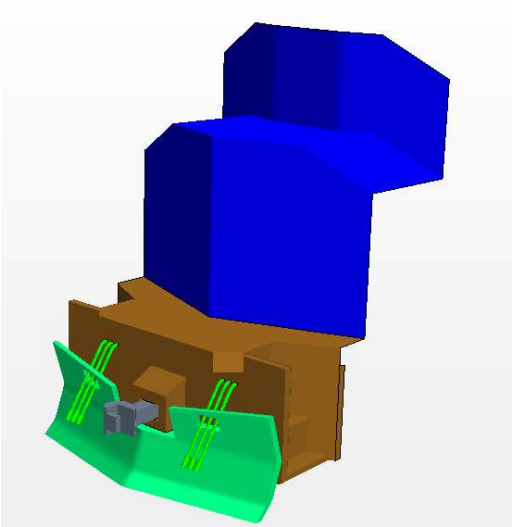

Figure 7. Named surfaces of component front

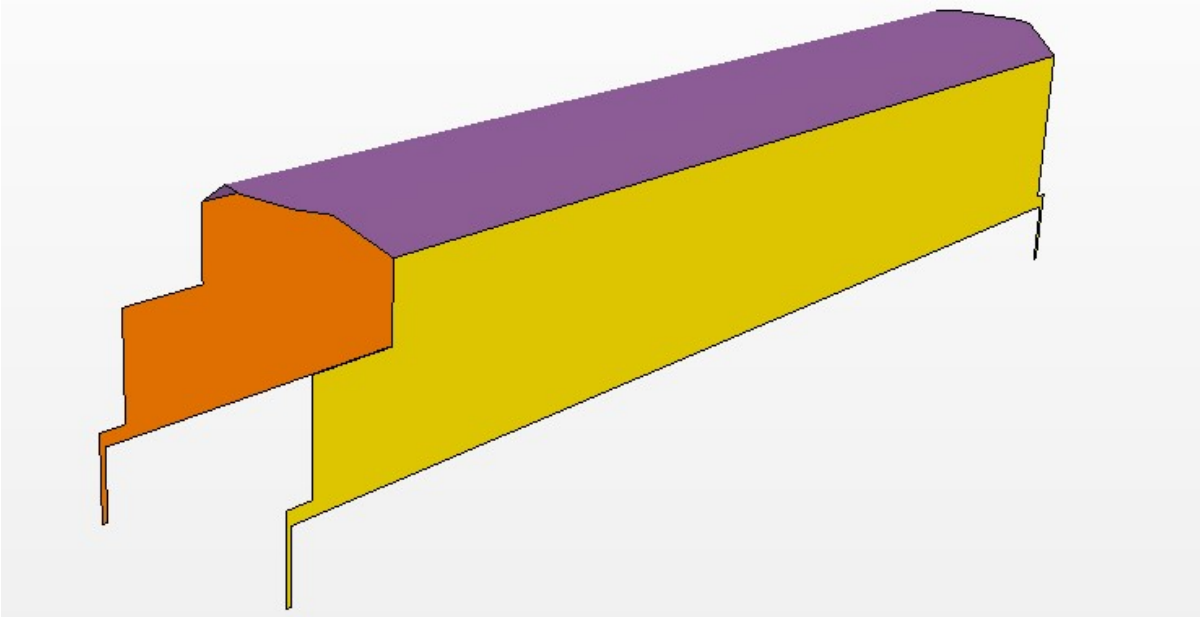

Figure 8. Named surfaces of component middle

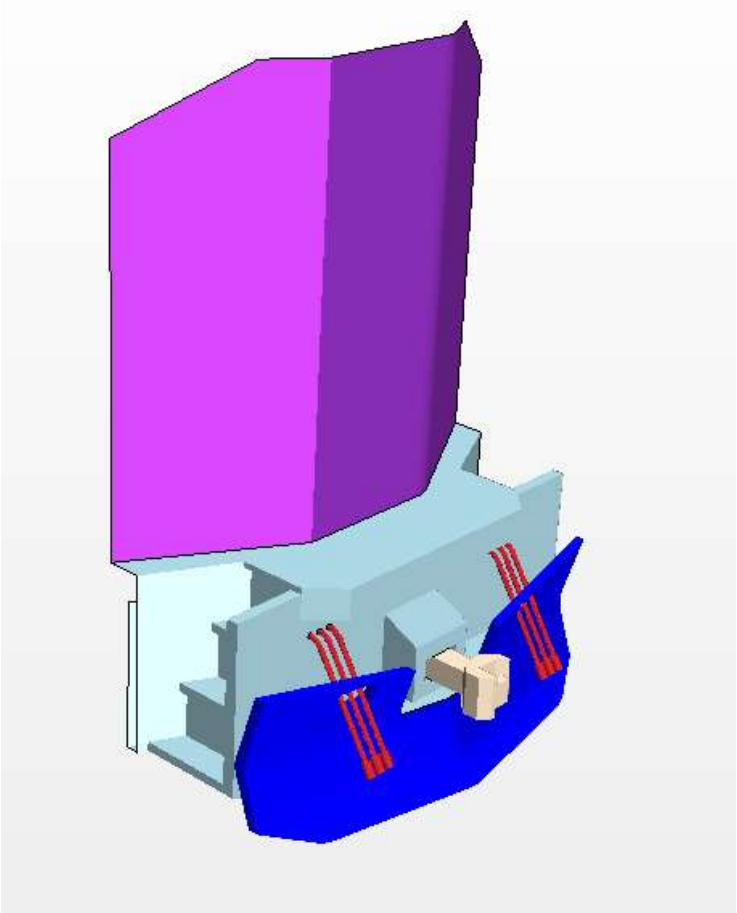

Figure 9. Named surfaces of component back

Figure 10. SD 40 bogie (Zehr 2016)

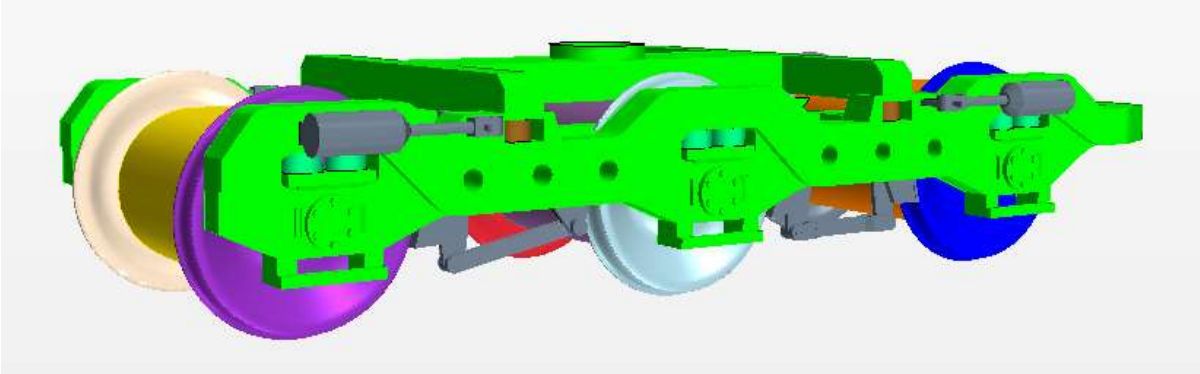

Figure 11. Named surfaces of component front bogie

Figure 12 shows the undercarriage which consists of the bottom of the deck and the fuel tank. This feature is also defeatured from a real model missing many small pieces such as fuel lines, valves and regulators that are mounted externally. The rear bogie is the same as the front bogie just spun 180 degrees. The rear bogie has the frame, engine cases, wheels, suspension, brakes, and brake lines. The wheels were modeled to AAR Manual of Standards and Recommended Practices Wheels and Axles M-107/M-208 Appendix B (Committee 2013). The real wheel profile was used to increase the fidelity of the simulation. Figure 13 shows the wheel profile that was used. The actual rail profile was chosen to increase the realism of the simulation. By using the rails there becomes a channel like flow underneath the train. Using the rail profile will allow for any real vortices to form and interact with the flow through the bogies. Figure 14 shows the rail profile that was used in the simulation.

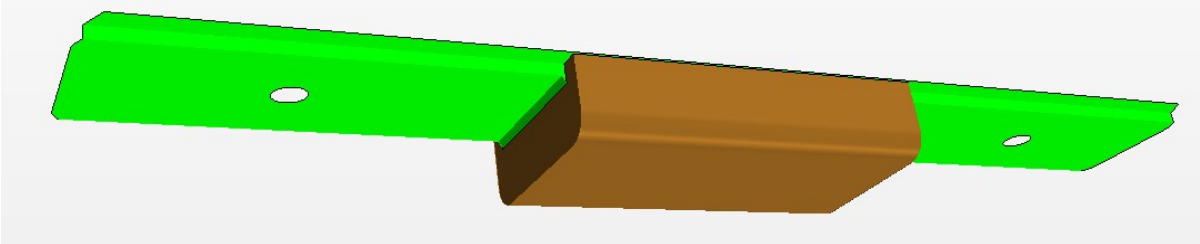

Figure 12. Named surfaces of component undercarriage

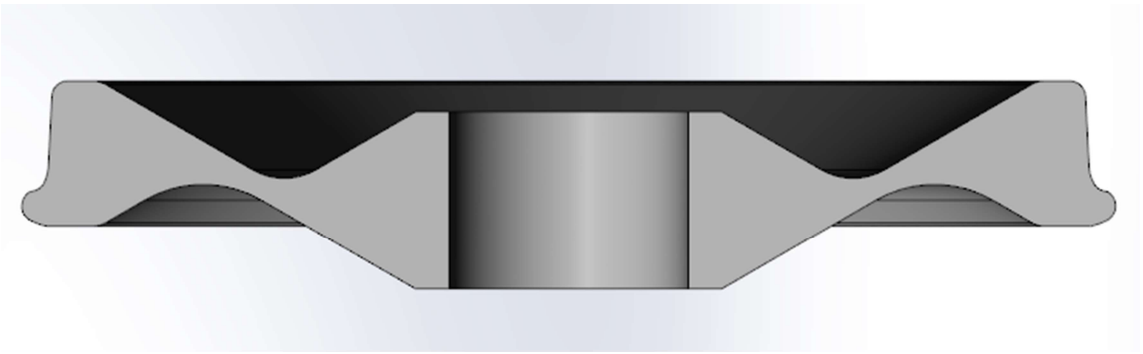

Figure 13. Wheel profile (rotated)

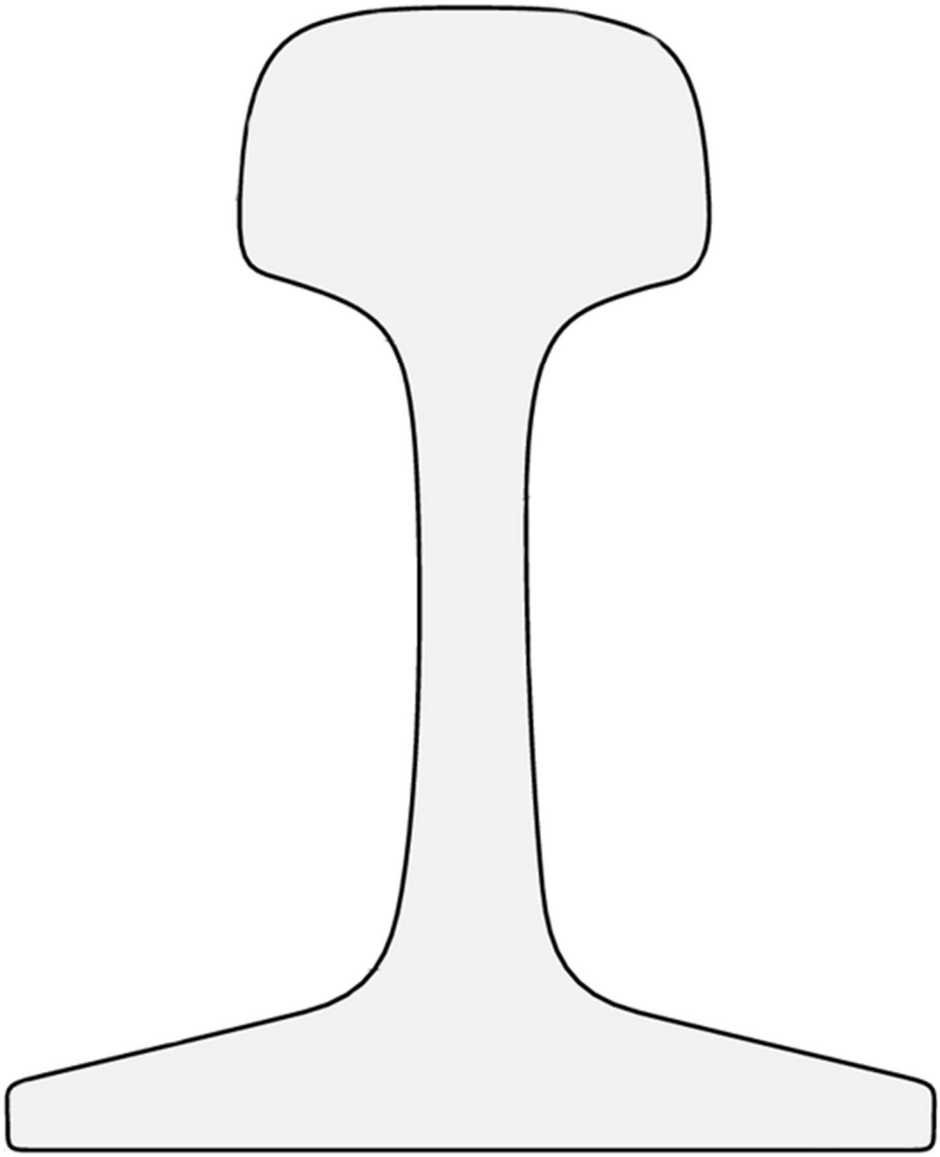

Figure 14. Typical rail profile used in simulation

3.3. Meshing

The domain was divided into different regions for meshing. The incoming flow region, before the train, has larger cells to reduce the cell count. The area by the train and in the wake, is refined to capture the flow features near them. The road bed is finely meshed the entire length to avoid having any shape transitions on the rails.

The advancing layer mesher was used because it gives a proper mesh for the boundary layer. How it works is, the surface mesh is extruded into the domain until it is the specified thickness and number of prism layers. Then the mesher computes the polyhedron mesh inside the domain. Figure 15 shows a top view of the mesh domain with specific features called out.

3.3.1. Cell Count Comparison to other works

The domain of the simulation has 40 million cells in it. In the refined region, a meter-long section of roadbed, 5 meters high, has ~1.2 million of cells. Due to the enormous number of cells in the field, refining the mesh to do a mesh refinement study to check grid independence of the solution is not possible on the currently available computing resources. Simplified train and locomotive simulations have approximately 4-7 million cells per car.

3.3.2. Far Field

The average cells size in the far field is 1.5 meters. The prism layer has 11 layers and is 3 mm thick. The coordinate system for the studies is as follows. X is parallel to the rails, is vertical, and Y is to the left if looking at the oncoming locomotive. The far field has a slip wall. All other walls are non-slip.

3.3.3. Bogies/Trucks

The bogies were very complex to get to mesh well. A scheme of picking the surface size of the named surfaces was used. Then the advancing layer polyhedron mesher took care of transitioning the sizes. In the table below you can see the size of the all the surfaces near the

bogies which will influence the size of the polyhedron mesh. Figure 16 shows three views of the bogies and their mesh.

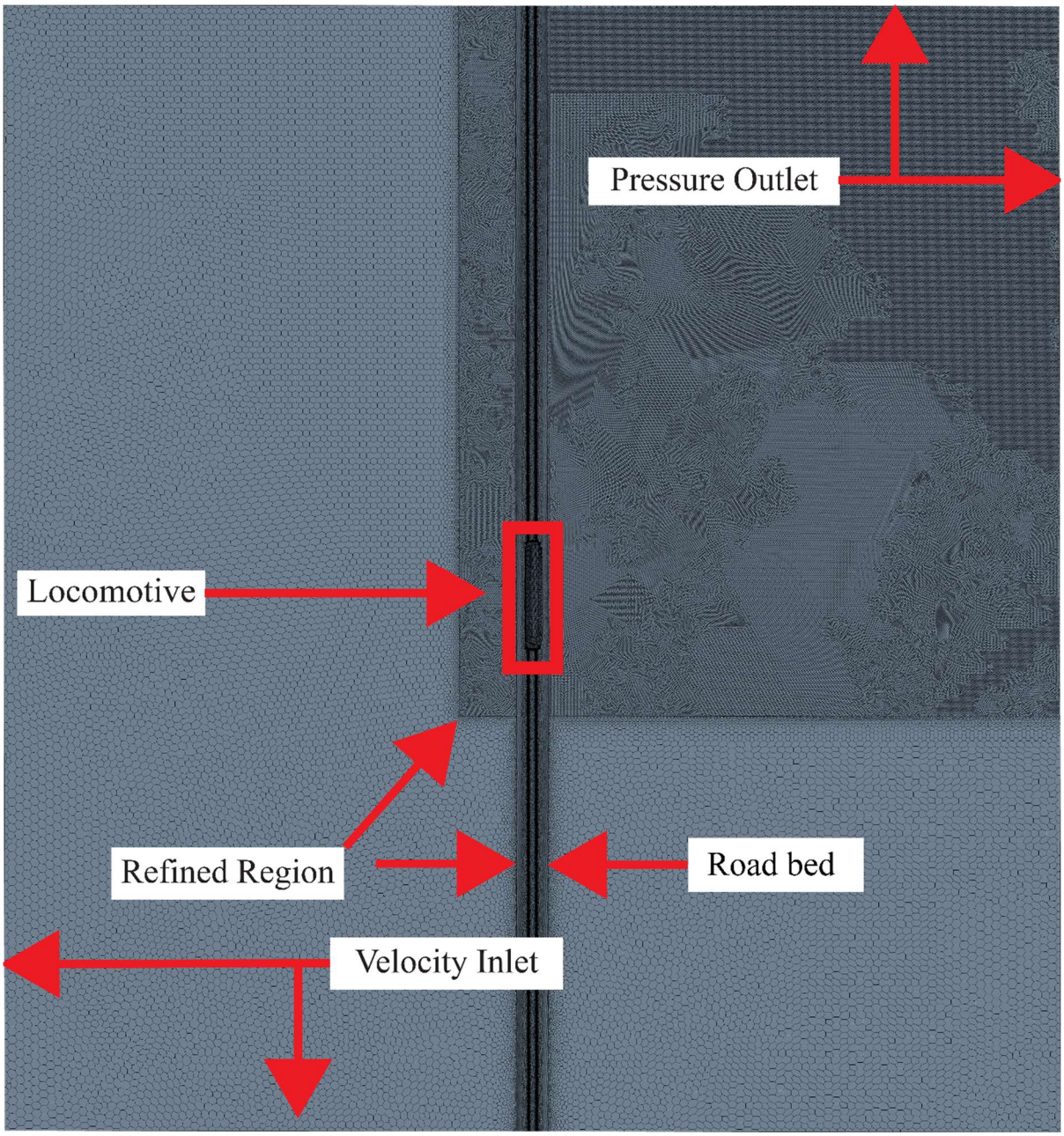

Figure 15. Domain mesh overview

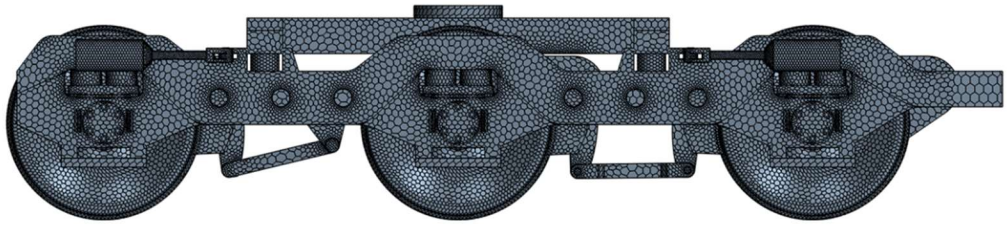

(a)

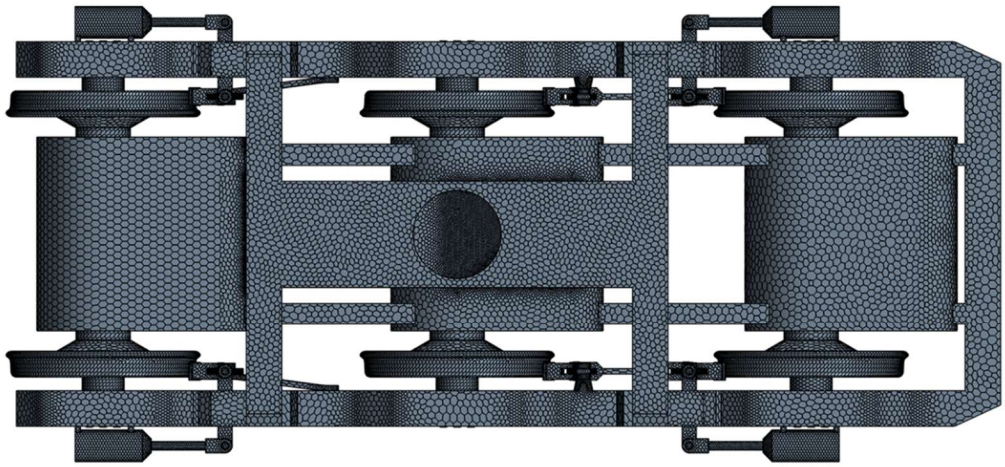

(b)

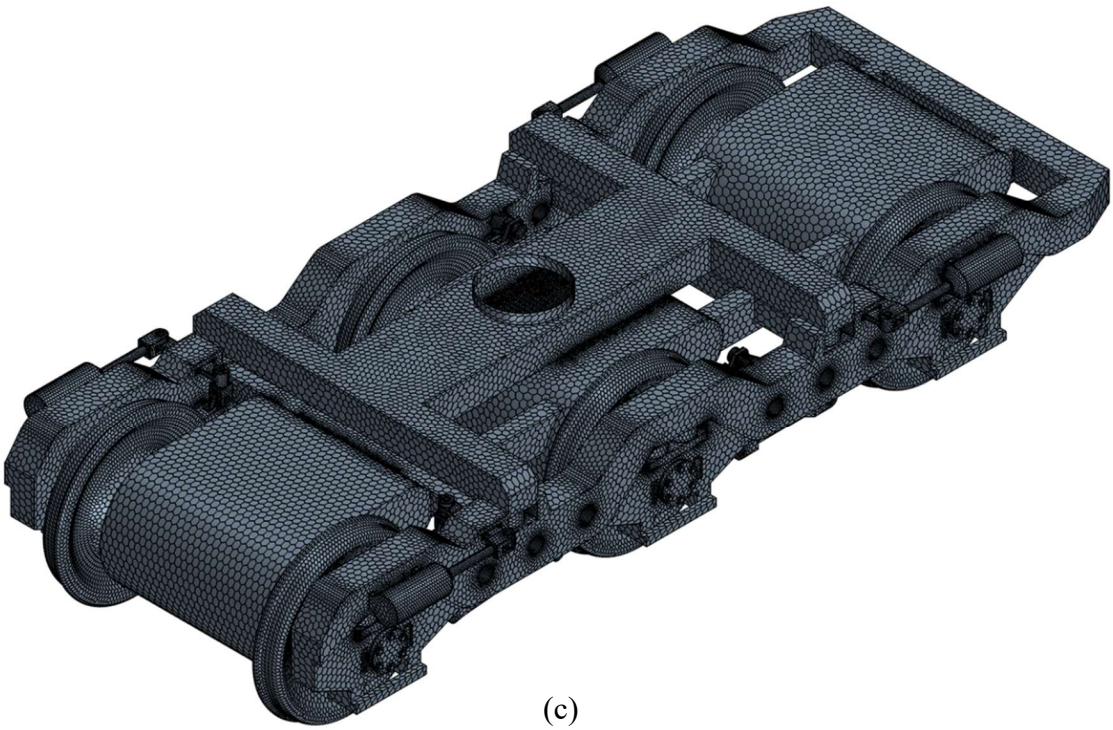

(c)

Figure 16. Bogie mesh (a) side view (b) top view (c) isometric view

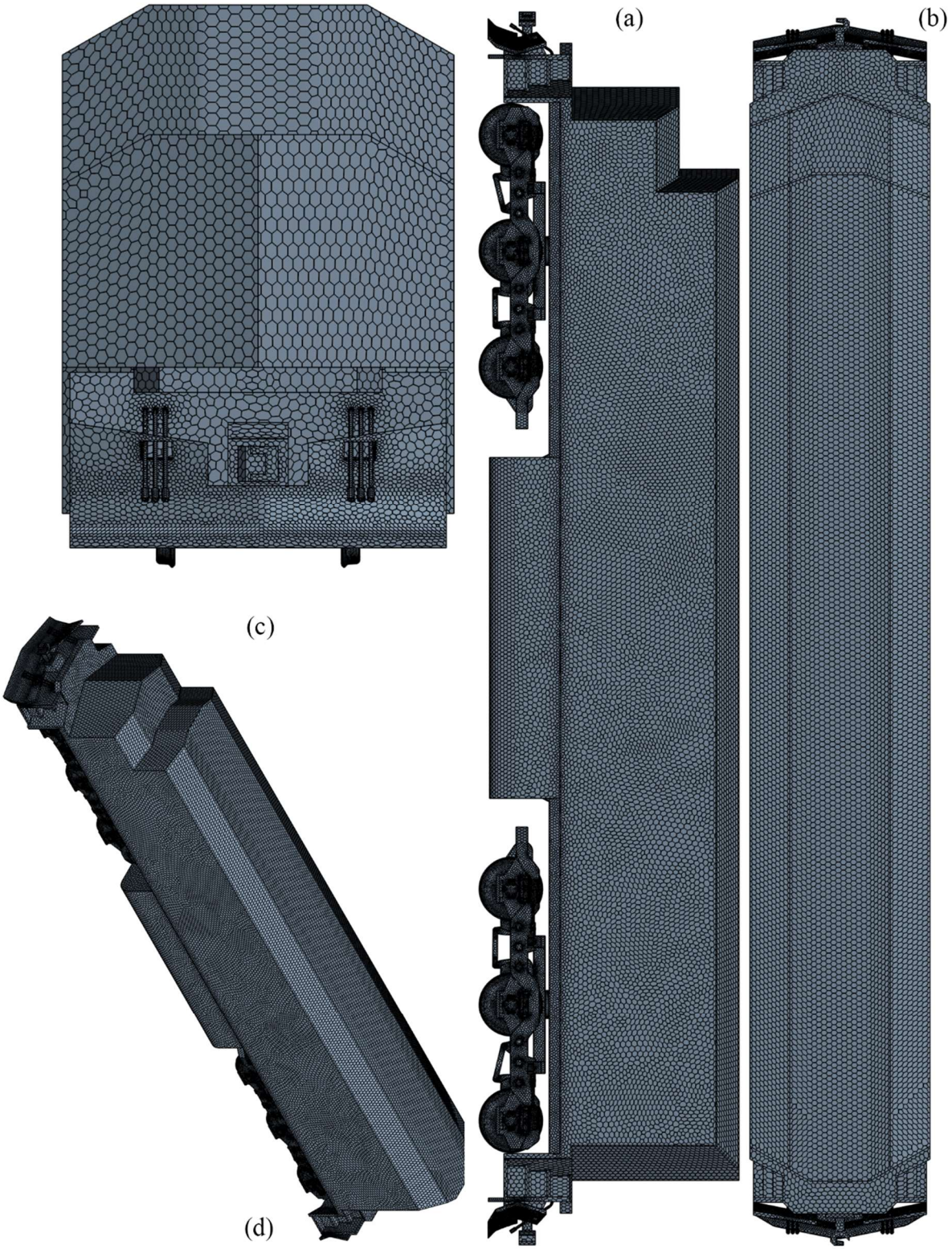

Figure 17. Locomotive mesh (a) side view (b) top view (c) front view (d) isometric view

3.3.4. Locomotive

The mesh on the upper surface was much easier to build. This was straight forward. A surface size of 7 cm was chosen. The prism layer on the locomotive was 3 mm. Figure 17 shows four views of the locomotive and the locomotives mesh.

3.3.5. Mesh Packing and Mesh Growth

The reason for the changing mesh sizes on the locomotive was to drive the total cell count to a manageable level. The more cells, the more memory required, the more CPU time required, and the more disk space required. The runtime increases with the number of cells squared. The graph (Figure 18) below shows the runtime for a simulation based on mesh size. Clearly it can be seen that as the cell count increase, the required computational time increases dramatically.

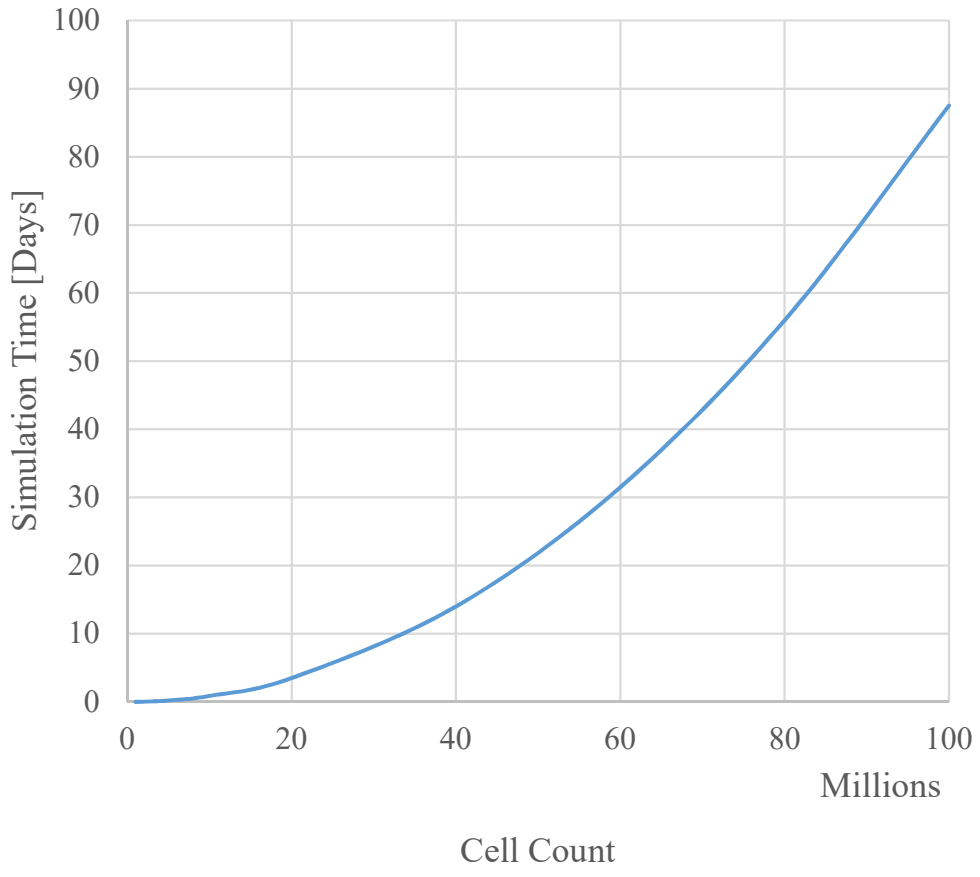

Figure 18. Cell count versus simulation time in days using 192 CPUs on cluster

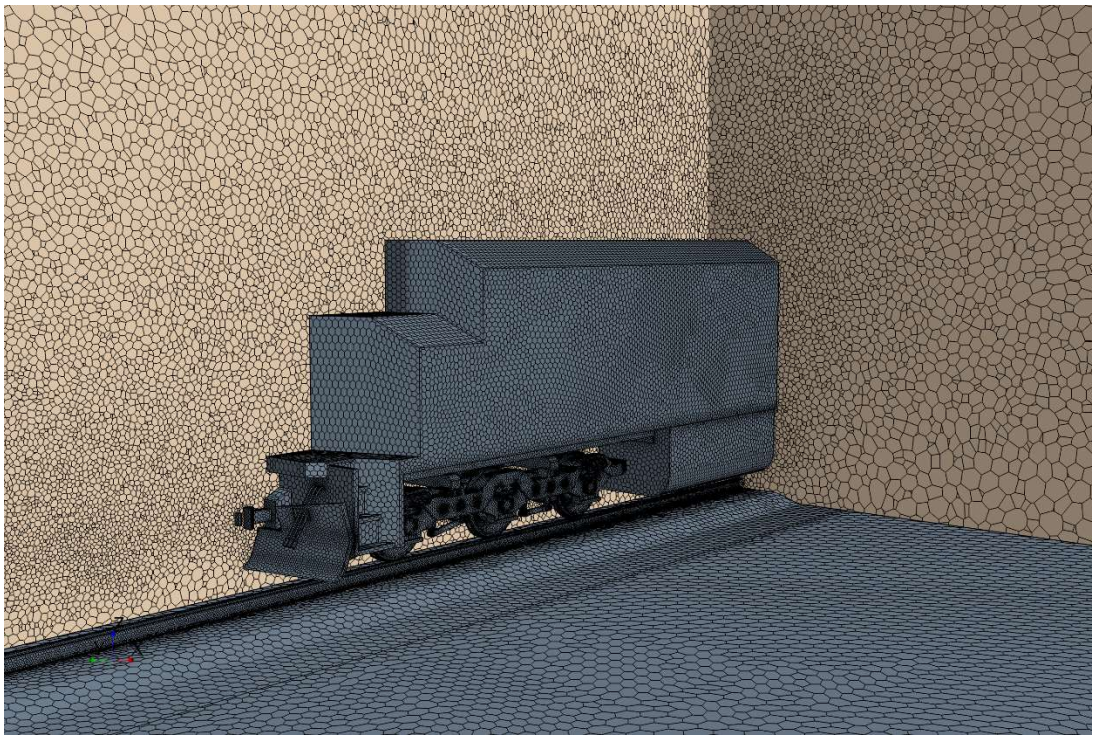

Figure 19. Cross planes of the grid near the locomotive surface

3.3.6. Cross Planes

The grid was packed near the vehicle to resolve any large-scale structures that maybe forming in the field. The grid is presented here with a plane down the center of the vehicle and the cross plane is down the center of the fuel tank. The grid gets larger the farther from the vehicle. Figure 19 shows a cross plane of the mesh down the center of the locomotive and across the middle of the tank.

3.3.7. Boundary Layer

The prism layers are used to resolve the boundary layer. To see if the mesh will accurately predict drag, y^+ has been calculated for the locomotive. The average y^+ value for the train is 2.87 for the max velocity case. All walls have y^+ treatment. (y^+ is a measure of how well the prism layer mesh is capturing the boundary layer).

3.3.8. Mesh Quality

To check if the quality of the mesh a visualization tool was built to see the bad cells in the domain to see if it was a surface mesh size issue or something else. The tool was built using according to the star user manual (CD-adapco 2016) Bad cells are cells that have one or more of the following issues: Cell Quality, Cell Warpage, Chevron Quality, Face Validity, Least Squares, Skewed Cells, and/or Volume Change. In below image the top image is a one meter rail section demonstrating the visualization abilities. The blue floating surfaces are cells that contain one issue. The regularity of the bad cells is a concern. The second image show the issue when resolved. Most of the mesh issues are within the prism layers. Figure 20 shows two images from the bad mesh visualization tool. Figure 20 (a) Shows consistent bad cells next the rail head and Figure 20 (b) shows the issue has been resolved.

3.4. Boundary Conditions

The boundary conditions for the simulation are the following. A uniform velocity inlet and constant pressure outlet. The ground and wheels will be discussed in more detail to elaborate on how the moving ground plane and rotating wheel conditions are applied. Table 1 shows the velocity and angles for each test condition.

3.4.1. Velocity Inlet

The velocity inlet is specified by giving the velocity magnitude and then a direction vector. These both change at each angle. The following table has the velocity magnitudes and direction vectors for each condition that was ran.

3.4.2. Moving Ground

The locomotive is moving relative to the ground in the observer reference frame but in the train reference plane the ground is moving relative to the train. To achieve the ground moving relative the train the roadbed was given a tangential velocity of 70 mph. The rails were also

given the tangential velocity. Figure 21 shows the profile of the roadbed. The rails were lifted from the ground because in most railroad ride of ways the rails are lifted up.

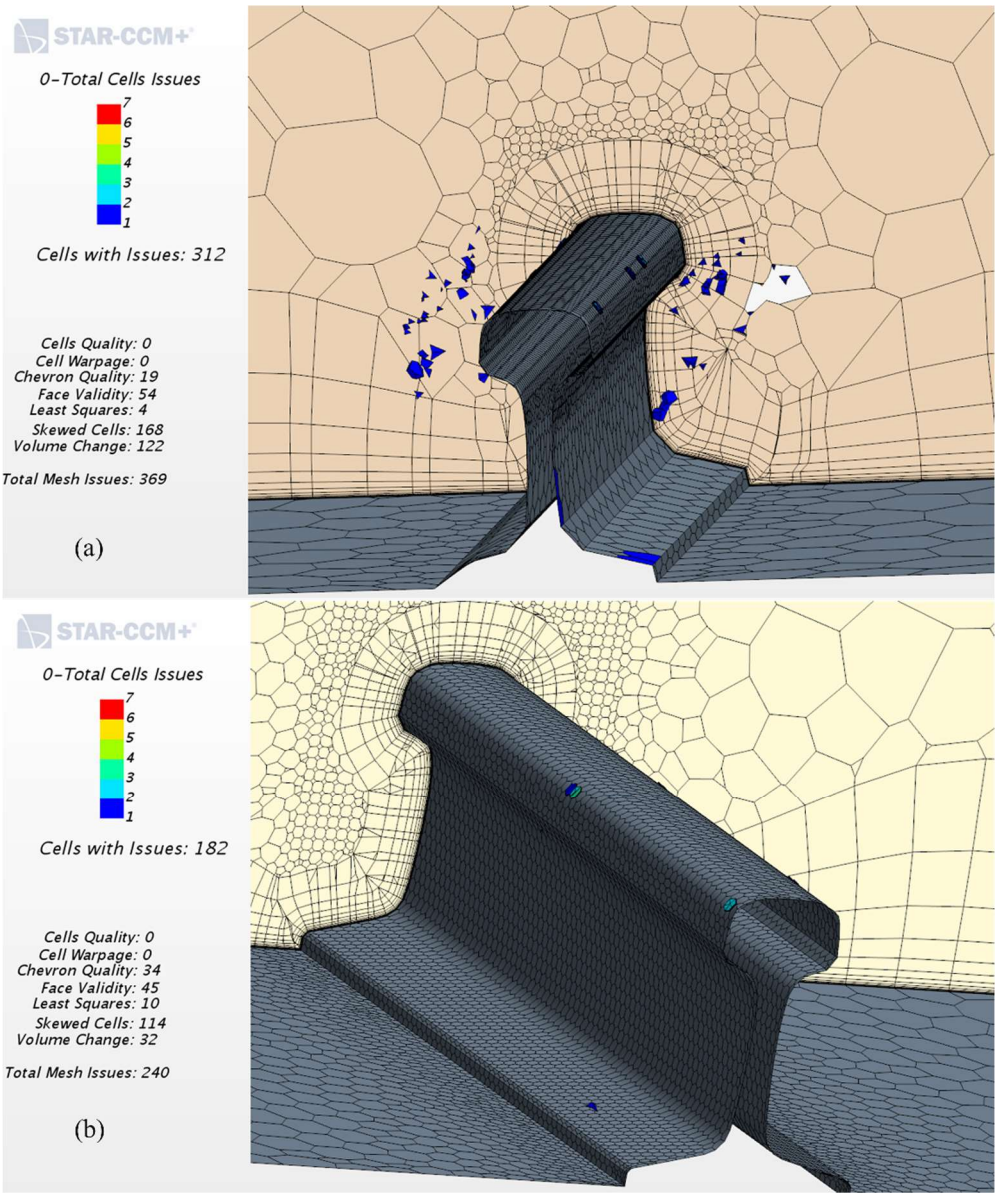

Figure 20. Bad mesh visualization tool (a) mesh with issue (b) mesh with less issues

Table 1. Wind speeds and wind angle

β [deg]	θ [deg]	U_∞ [MPH]	U_x [MPH]	U_y [MPH]
-0	0	105	105	0
-15	-4.99	104	103.8	-9.1
-30	-9.90	102	100.3	-17.5
-45	-14.64	98	94.7	-24.7
-60	-19.11	93	87.5	-30.3
-75	-23.15	86	79.1	-33.8
-90	-26.57	78	70.0	-35.0
-105	-29.02	70	60.9	-33.8
-120	-30	61	52.5	-30.3
-135	-28.68	52	45.3	-24.7
-150	-23.79	43	39.7	-17.5

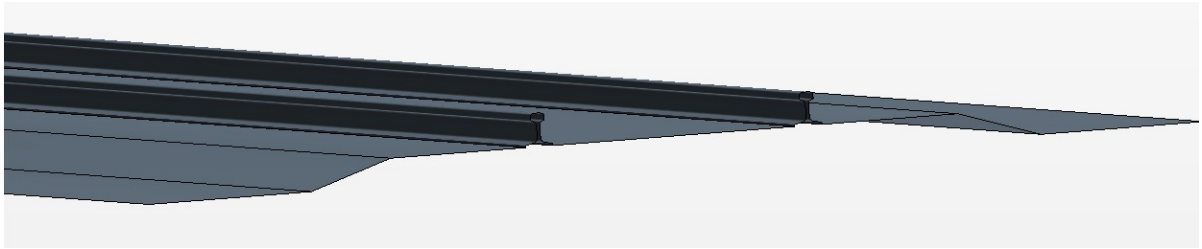

Figure 21. Roadbed cross section

3.4.3. Rotating Wheels

Star-CCM+'s best practice for rotating wheels says if the wheels are axisymmetric then an angular rotation rate can be applied to the center of the wheel (CD-adapco 2016). The center of each wheel was then found and the tangent velocity of the wheel was set to 70 mph and the correct angular velocity was calculated and applied. The wheels of the locomotive were lifted from the rails by 1 cm. This was to ensure the wheels were axisymmetric. The angular rotation assumption does not work for non-bodies of revolution.

3.5. Solver Convergence

To verify that the solution has reached a steady state solution, three criteria were applied: residual should drop at least two of orders of magnitude, simulation time should be at least three times the free stream velocity divided by the length of the vehicles, and the average force value should have become a constant value. Table 2 shows how long each simulation has in the solution space time and the number of times the flow has gone past the locomotive.

3.5.1. Residual Drop

The residuals do drop half an order of magnitude but do oscillate. The simulation was started by having an initial condition of all the flow moving at the freestream speed and direction then an Euler solver runs over 9 levels of mesh refinement starting with course and ending on the actual grid. Figure 22 shows how the residuals drop and then oscillate. This gives a very good starting point for a solution problem where most of the flow is incompressible. The other reason the residuals do not drop is the large flow separation region on the vehicle. To guarantee the flow has stabilized a force average is used.

Table 2. Convergence conditions

Wind Angle Degrees	Iterations	Time	Flow Passes
-0	12250	1.04	2.3
-15	14750	1.25	2.8
-30	15000	1.27	2.8
-45	14304	1.21	2.5
-60	20250	1.72	3.4
-75	28750	2.44	4.5
-90	18250	1.55	2.6
-105	22000	1.87	2.8
-120	20000	1.70	2.2
-135	19750	1.68	1.8
-150	26000	2.21	2.0

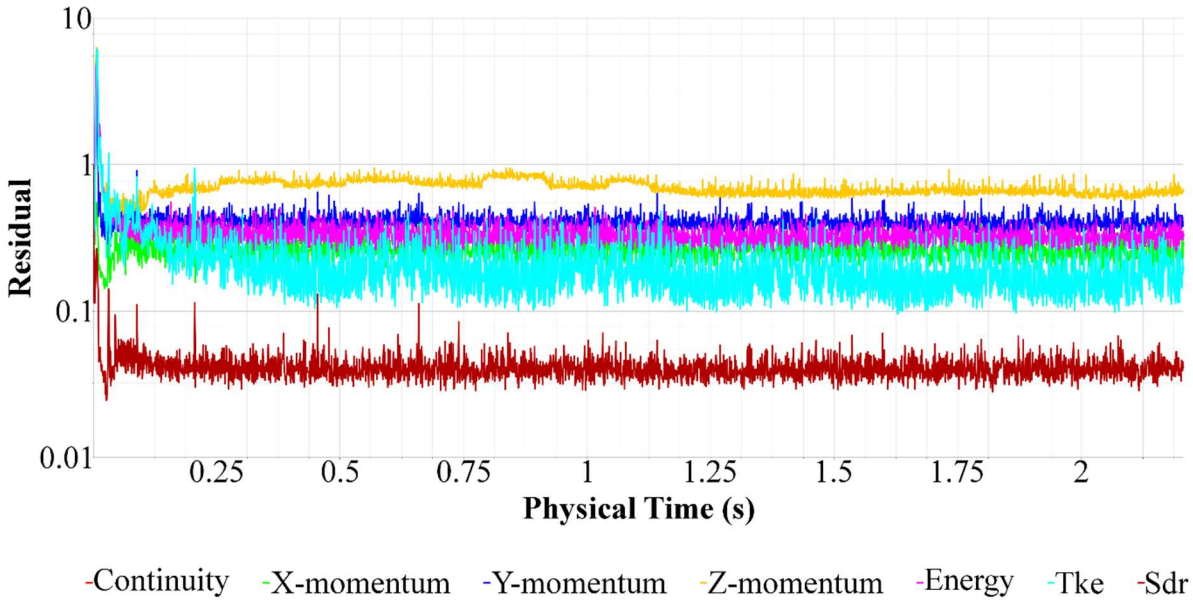

Figure 22. Typical residual plot for the flow solver

3.5.2. Force Value Averaging

The lift, drag, and side-force values were used to verify the solution had reached a steady value. The steady value is taken as the average of the force value over the past 8,000 iterations. This is done because of the oscillatory nature of the forces on the locomotive due to the unsteadiness of the vortex structures. Notice in Figure 23 the force values have a periodic oscillation. The forces usually start oscillating about their mean by iteration 5,000 or ~425 milliseconds. Using the rule of thumb for URANs convergence this simulation is converged. Due to the amount of wall time it would take to run all models to seven flows past the vehicle, the simulations were truncated sooner but still allowing for the oscillations to become steady. Figure 23 shows how the forces oscillate but start to oscillate about a constant value.

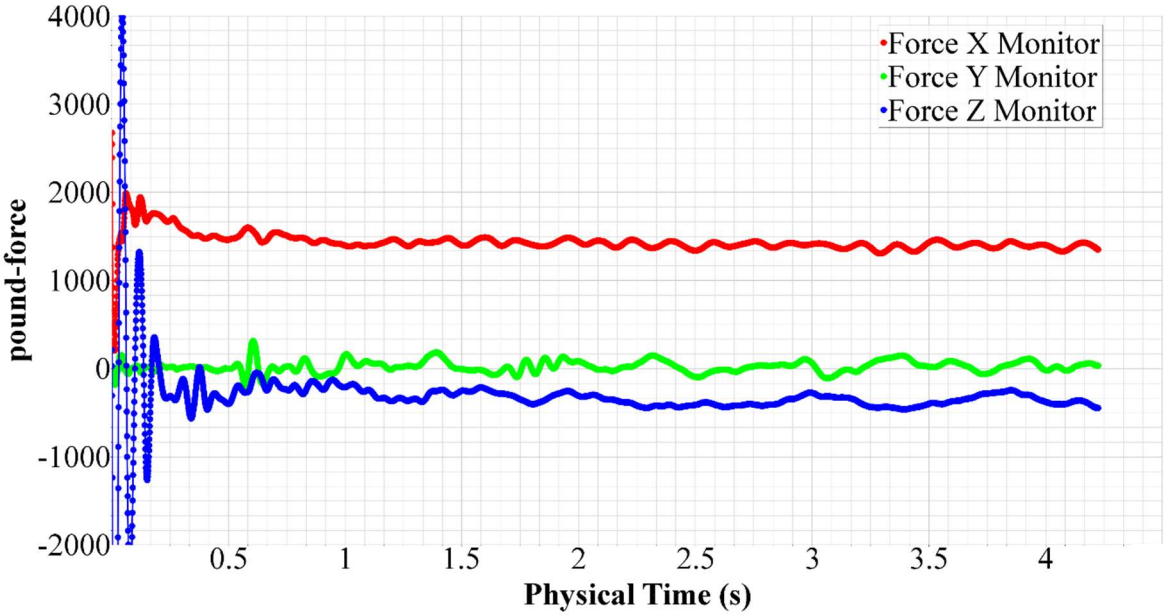

Figure 23. Flow solver history of the force value versus time

CHAPTER 4. RESULTS

The chapter presents results of the CFD studies. In particular, a description of the study is given first and the forces and drag components as a function of the wind direction angle and described. Visualization of the flow structures are also given and discussed.

4.1. Description of Study

The study will investigate the effects of crosswind on a locomotive. The locomotive has detailed geometry trucks. The total drag will be broken into components. The lift (C_L), drag (C_D) and side force (C_{SF}) coefficients will be presented for the entire locomotive. The wind direction angle (β) will be changed from 0° to -150° in -15° increments. While doing this, the speed of the wind is held constant. The magnitude of the velocity will be decreasing as the crosswind angle decreases. Figure 4 presents the change in velocity as a function of the angles. The study will also present flow field data from around the locomotive.

4.2. Total Locomotive Forces

When the forces are plotted, in Figure 24, an interesting result appears. The drag coefficient appears to be asymptotic. The lift force is also interesting, initially there is down force but as the wind angle increase lift starts to be generated. The side force coefficient is linear which is expected. When the x component drag coefficient is plotted against the Davis-Peters equation (2), a general agreement in the trend is there but more drag is predicted using CFD. The pie charts on Figure 25 is drag broken down into components. The components are presented in Figure 26 and Figure 27. The bars above and below the points are the plot are the maximum and minimum from the oscillations in the forces. Ideally, the Davis-Peters equation would run through the dots but if it is inside the bars the fit is acceptable. Looking at Figure 28 there is a misalignment of (C_{D_U})with the Davis-Peters equation when looking when plotted against the

crosswind angle. The stepper slope that CFD predicated could be due to a better drag prediction because the Davis-Peters equation was generated using only wind tunnel results.

4.3. Components of Drag on Locomotive with Crosswind

From the breakdown of (C_D) into the components, the components with the largest contributions are the front of the locomotive and the back of the locomotive. The front of the locomotive varies in its contribution from 75% to 40%. The back of the locomotive varies from just under 25% to 40% at its peak. The front of the locomotives contributions steadily decreases whilst the contribution from the rear of the locomotive increases. The bogies combined contribute no more than 15% and at a minimum 3% of the drag.

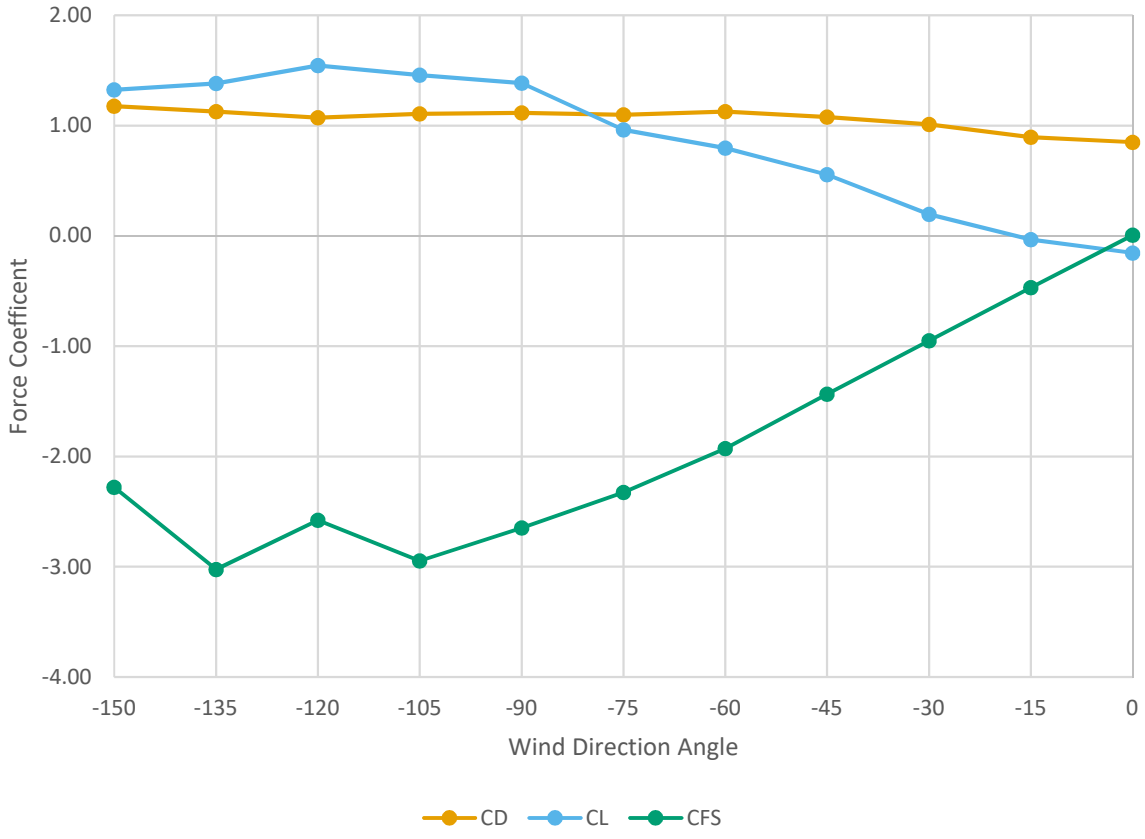

Figure 24. Force coefficient versus wind direction angle

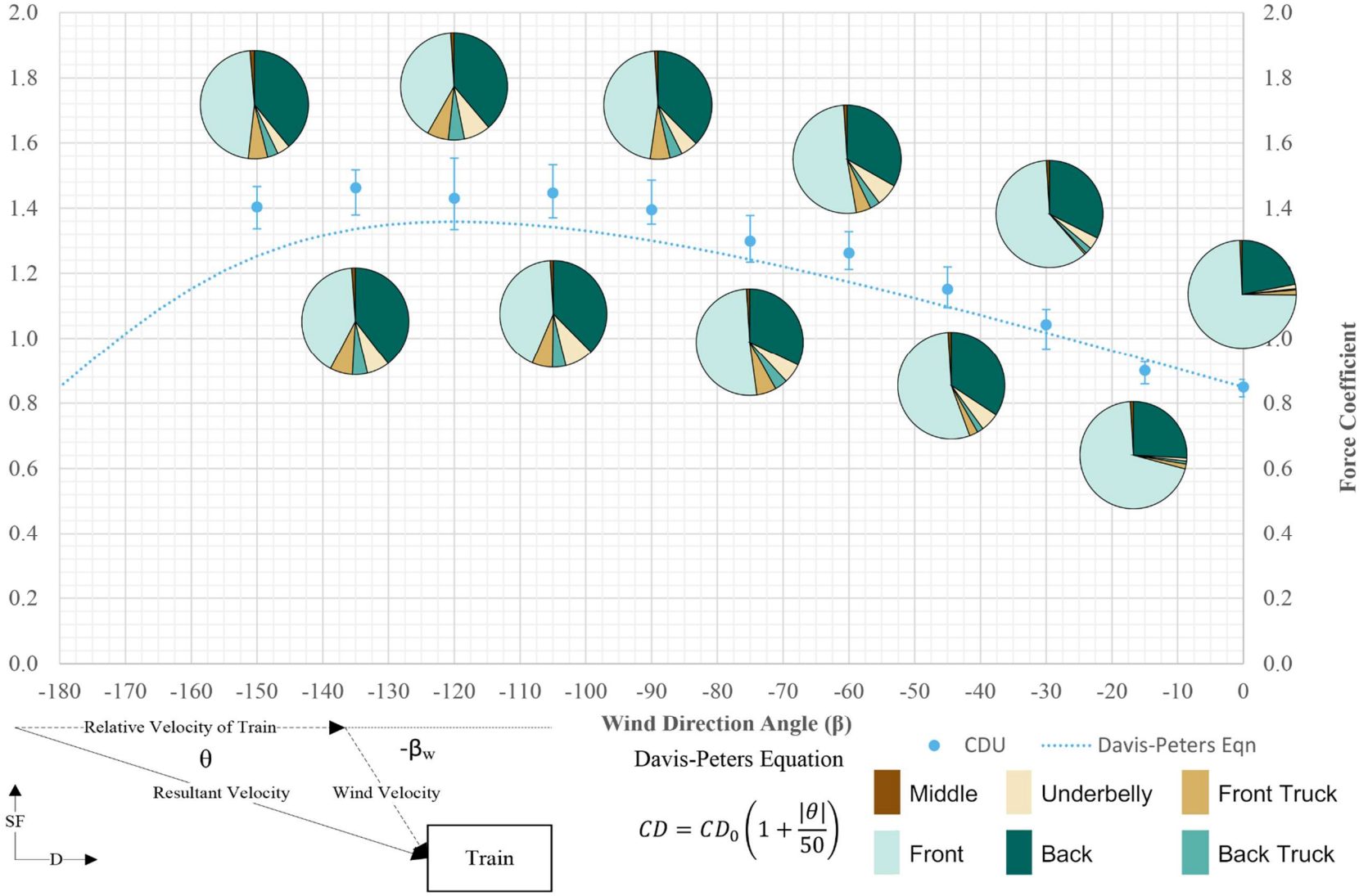

Figure 25. Coefficient of drag nondimensionalized by velocity along the rail versus wind direction angle

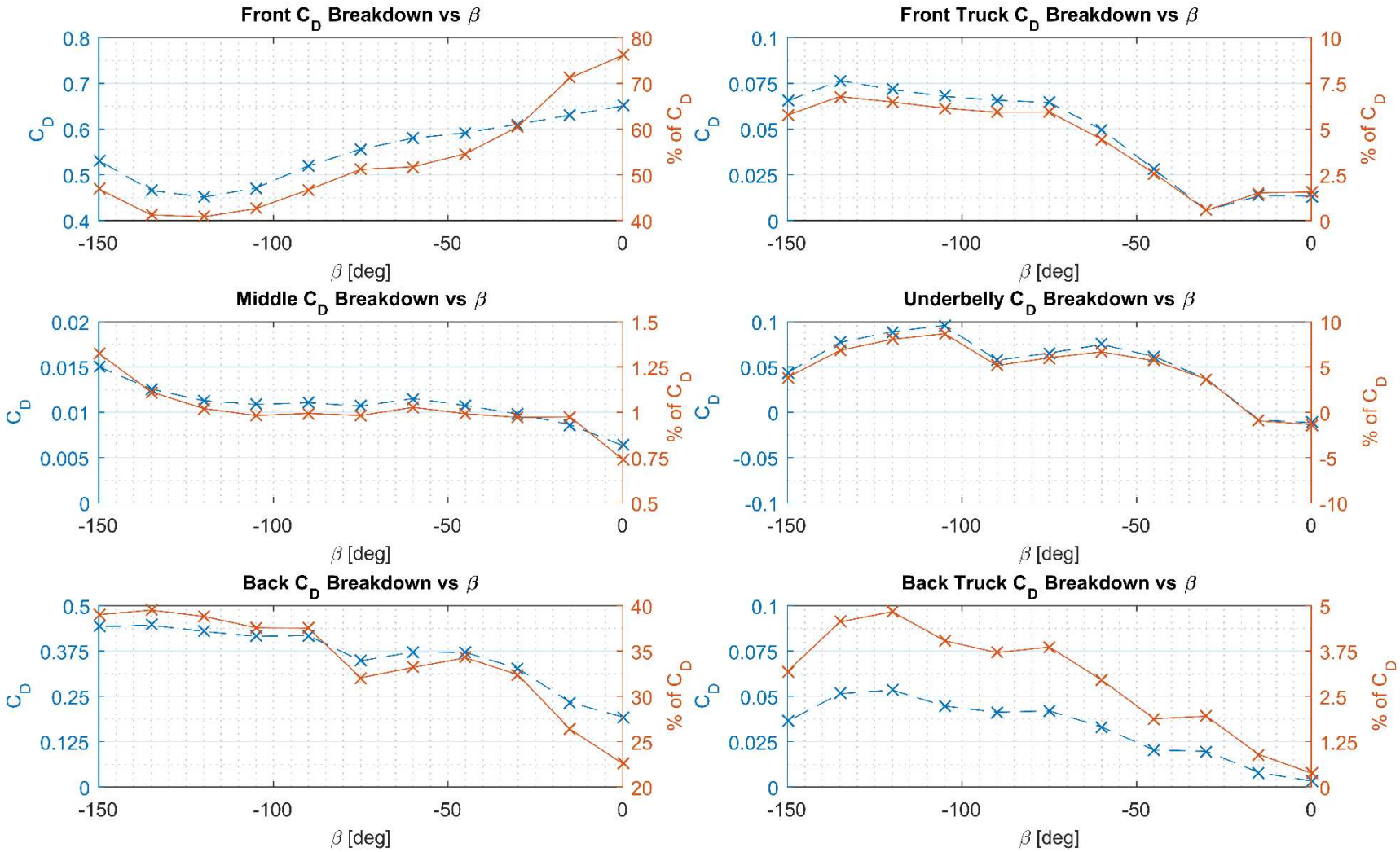

Figure 26. Drag nondimensionalized by rail direction velocity broken down versus wind direction angle

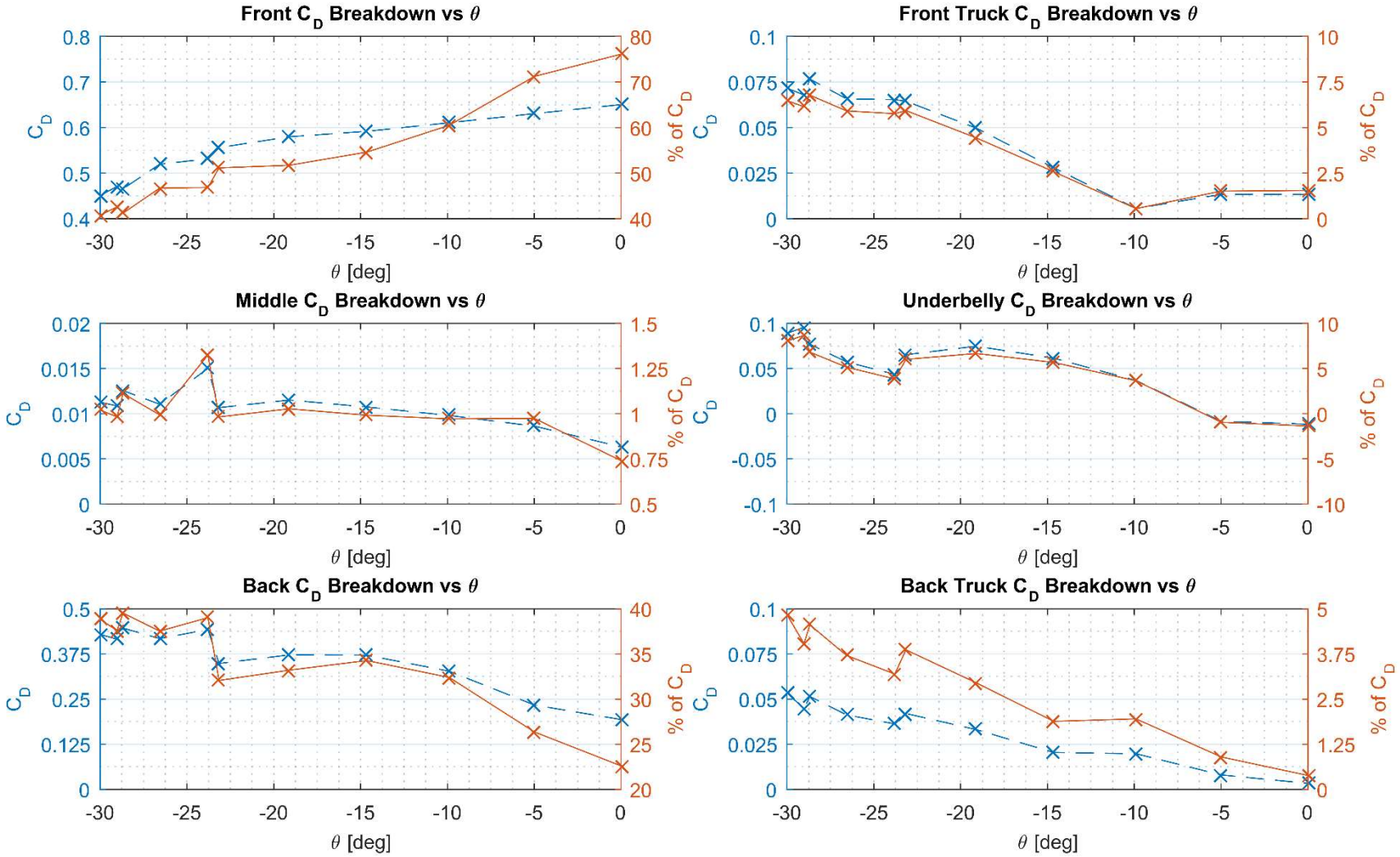

Figure 27. Drag nondimensionalized by total velocity broken down versus crosswind angle

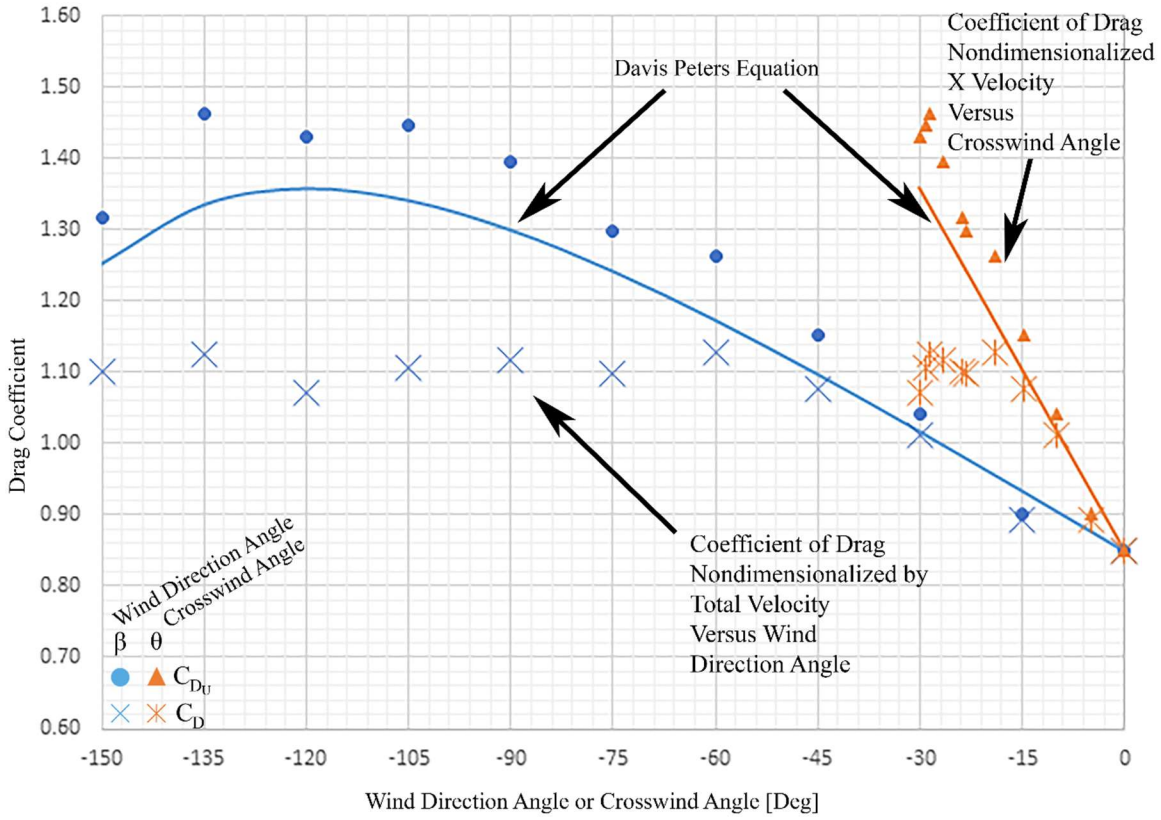

Figure 28. Comparison of nondimensionalization methods, plotted against wind direction angle and crosswind angle.

The back drag continues its trend at that point unlike the underbelly, middle and bogies. A cause of this could be the flow passes through the trucks with less obstruction due to the angle of the flow. This would lead to the vortex shifting its position forward and upward, causing it to act on the front and side of the locomotive. This trend is also observed in when the results are looked at verse the crosswind angle, except it appears the trends are very linear up to the maximum crosswind angle.

4.4. Beta Versus Theta for Results

Breaking down the results using different coefficients and angles results in different trends. When using (C_{D_u}) and the crosswind angle the trend appears linear but when using (C_D), the trend linearly rises to a point then levels off. This same trend is seen for the wind direction

angle. The Davis Peters equation appears to have a different slope than the data presented in Figure 28.

4.5. Discussion of Results

The front of the train resembles a frontward facing step that has been cut with two symmetric miters. The miters can be seen in Figure 17 (c), they are the leading part of the locomotive above the stairs. This presents a more aerodynamically efficient surface than if it were just a blunt square face. The miters are at a shallow angle causing a large turning angle for the flow and rather than staying attached to the wall the flow separates and causes a recirculation region. The can be seen using Figure 29 and Figure 30.

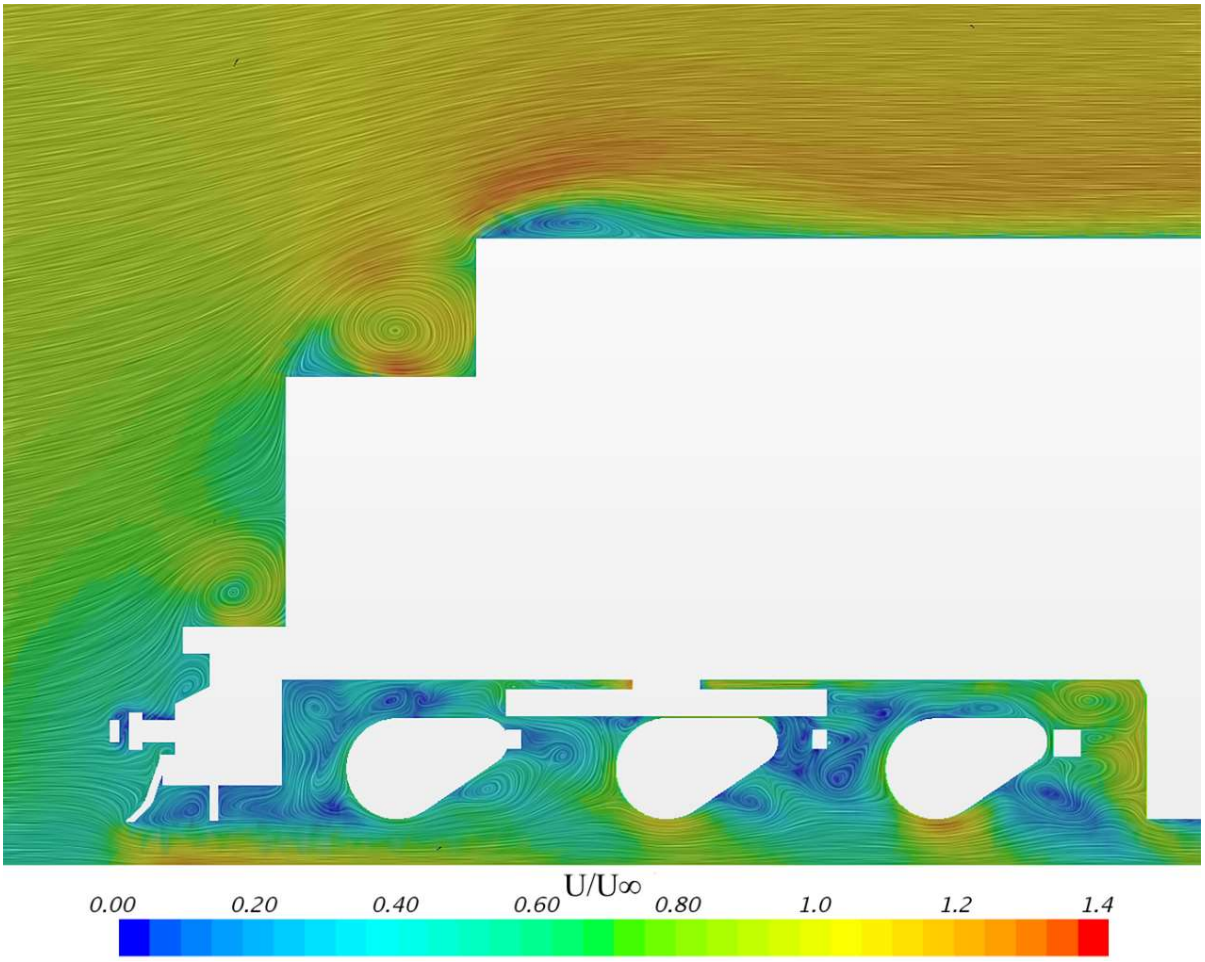

Figure 29. Cross section of centerline plane with streamlines of velocity/free stream velocity [-75 deg]

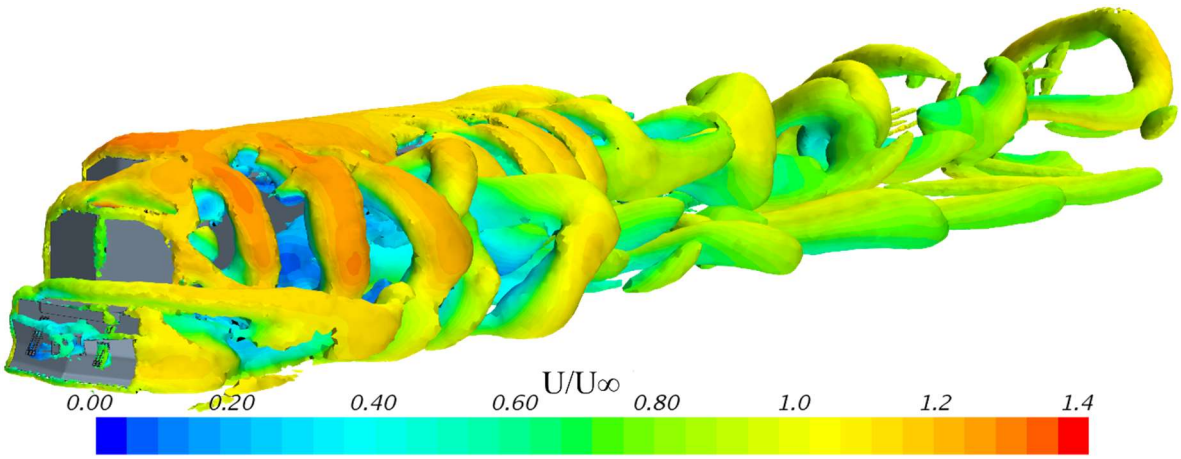

Figure 30. Vortical structure on leeward side [-75 deg]

This region is pushed with the crosswind until it separates, but now has a vortical component. The vortical component causes the flow to rotate and it meets the flow from the step below and they combine to form a vortex. The flow over the top of the train also separates because the turning angle is too great. On the leeward side of the locomotive a large vortical structure forms. This structure whips up and down and side to side shedding vortices. This vortex causes the forces on the locomotive to vary with time (see Figure 23, Figure 30, Figure 33, and Figure 34). This vortex is larger than the flow separation from the rear of the locomotive (see Figure 31).

There is a recirculation region above the bogies. The region exists from the flow going under the train meeting the fuel tank and turning into the bottom of the undercarriage then flowing over top of the bogies. The flow then drops back into the lower stream by going down between the motor casings. As the crosswind angle increases the flow still recirculates but some of the air is forced out the leeward side of the bogie. There appears to be a flow angle where the bogies have less resistance due to the flow passing more smoothly through the bogies. Figure 32 shows the flow passing through the bogies. When the flow is head on, the train sheds vortices on both sides in a buffeting fashion. This leads to the boundary layer on

the top of the train to have a unique wave like shape. This buffeting is reduced and the boundary layer becomes more uniform when a crosswind is introduced. This buffeting is moved to the leeward side of the car as seen in Figure 30.

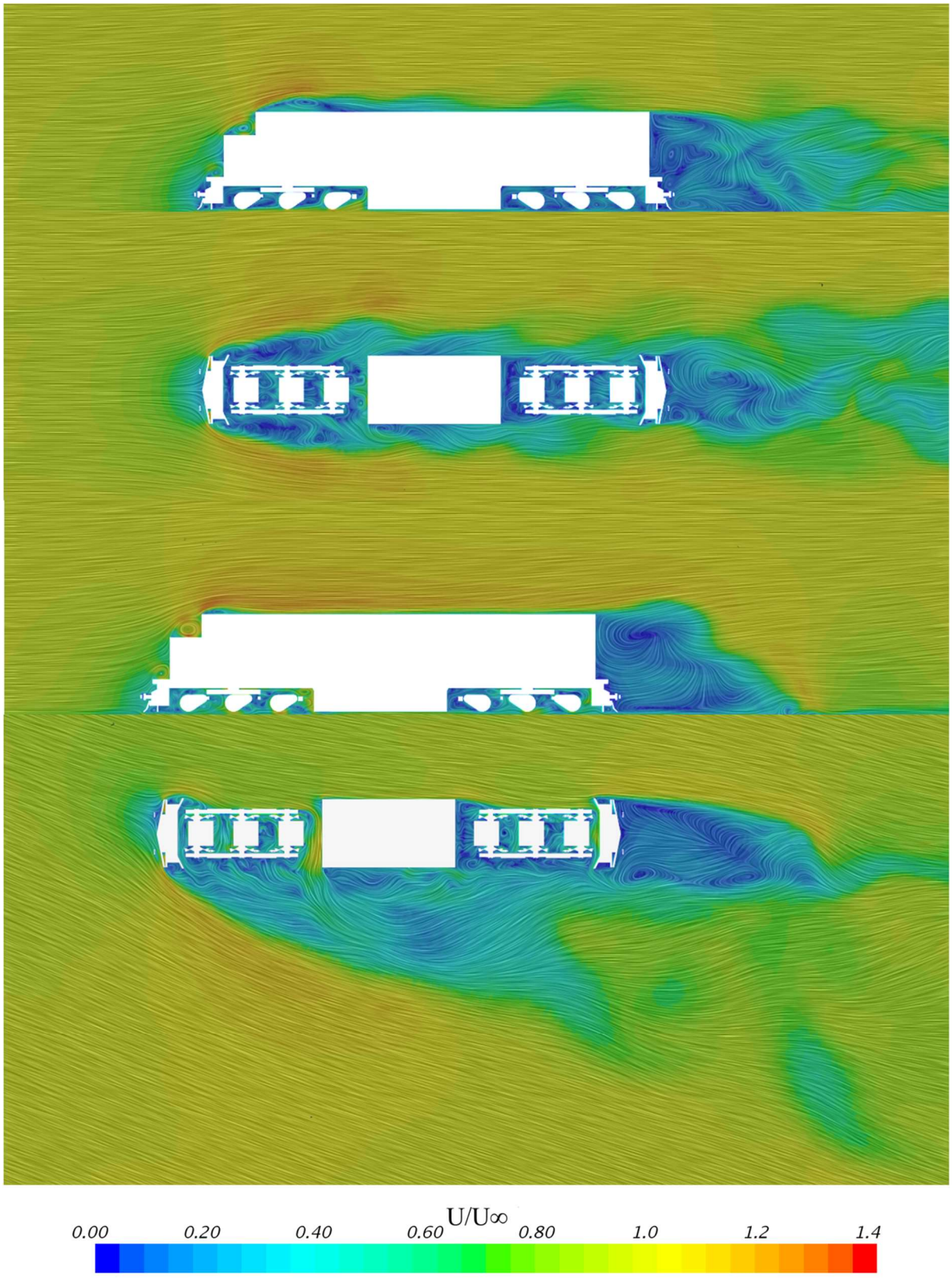

Figure 31. Streamlines of velocity on centerline plane of the vehicle and the center of the bogie [0 deg/-75 deg]

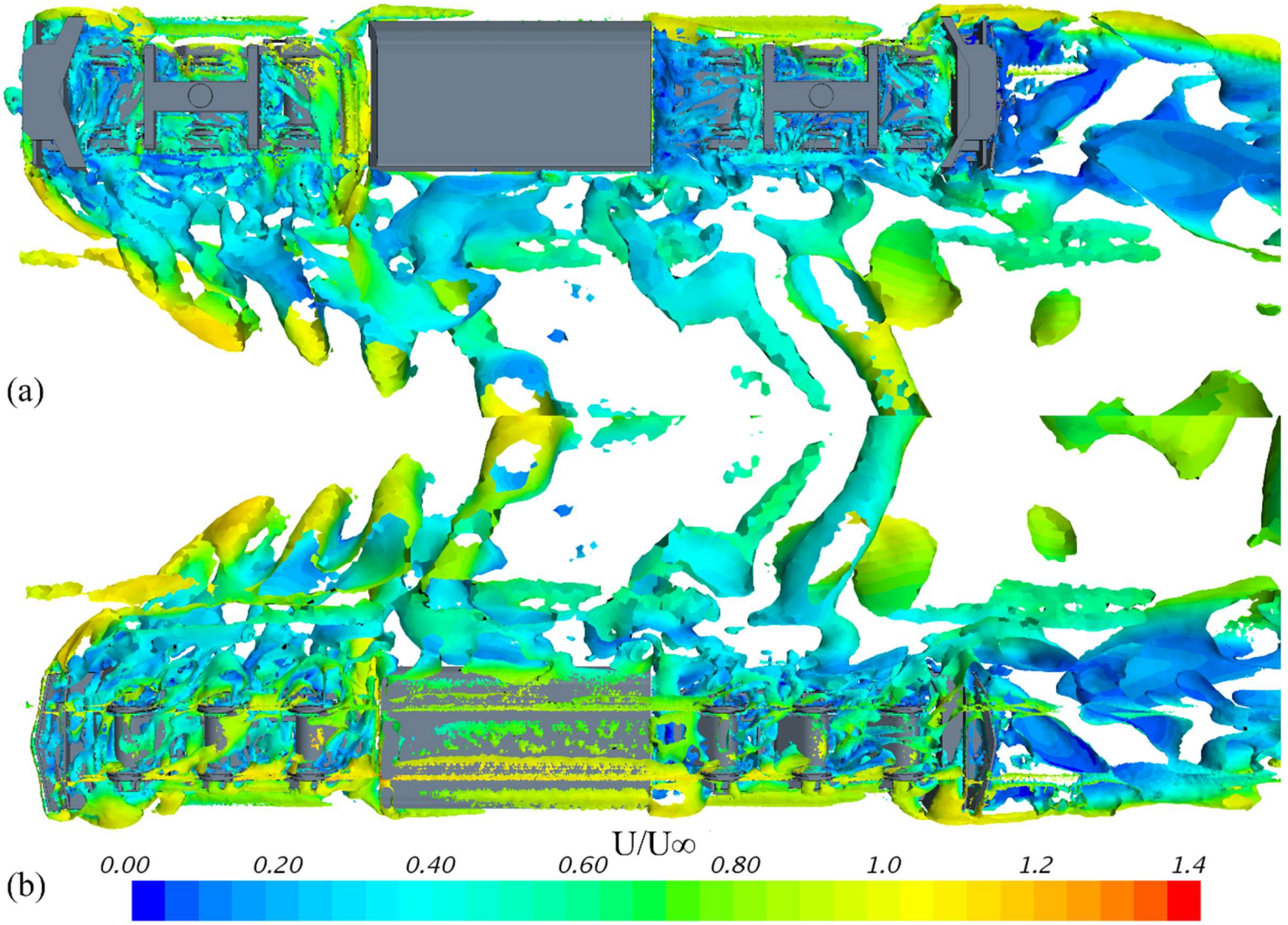

Figure 32. Bogie Q-Criterion with isosurface clip above 1.5m from roadbed (a) from top (b) from bottom

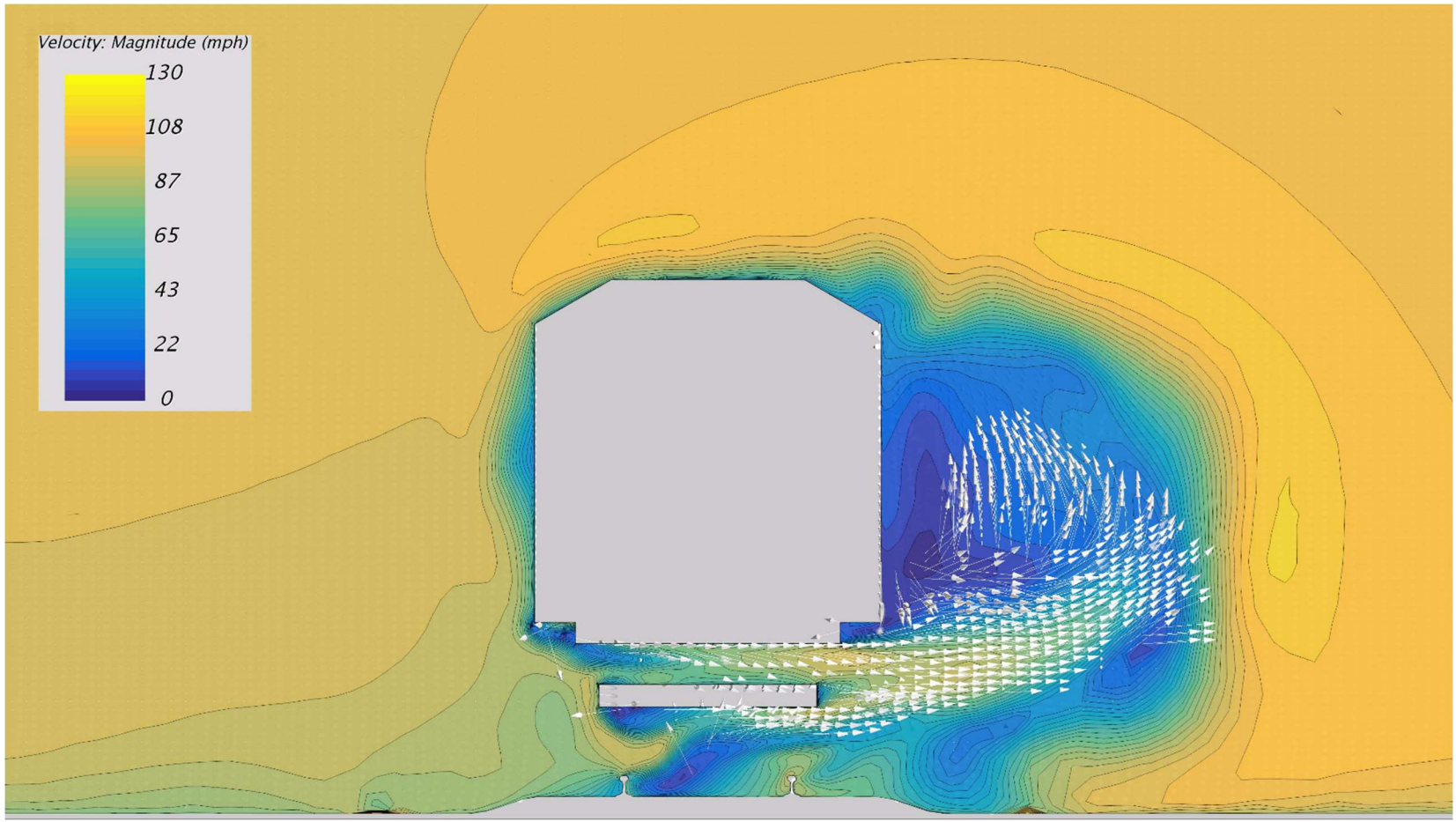

Figure 33. Section of Flow with Direction Vectors. Visible Arrowheads Indicate Flow Traveling Out of Page [-45 deg]

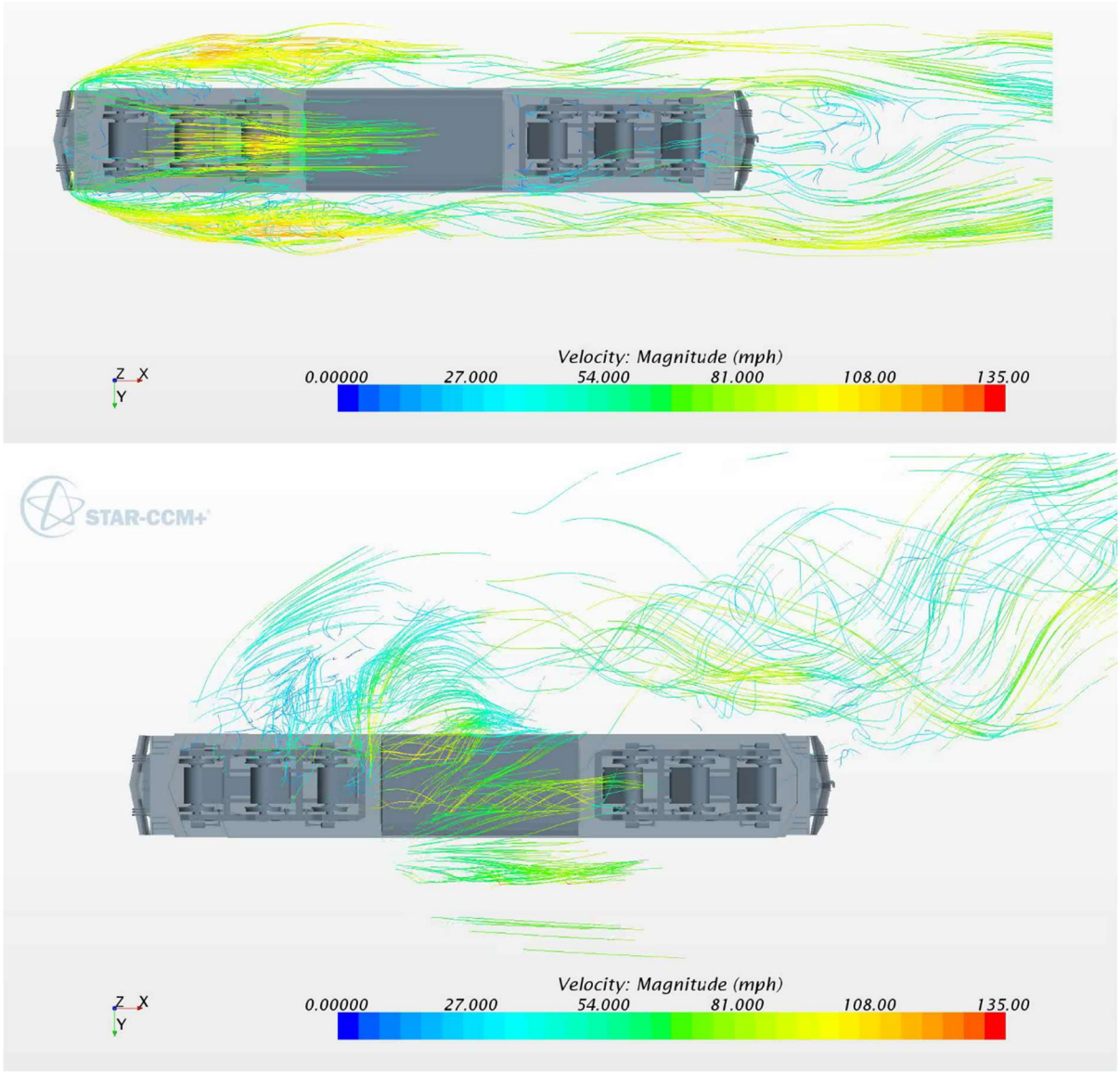

Figure 34. Streamlines of Undercarriage [0/-45 deg] View From Bottom

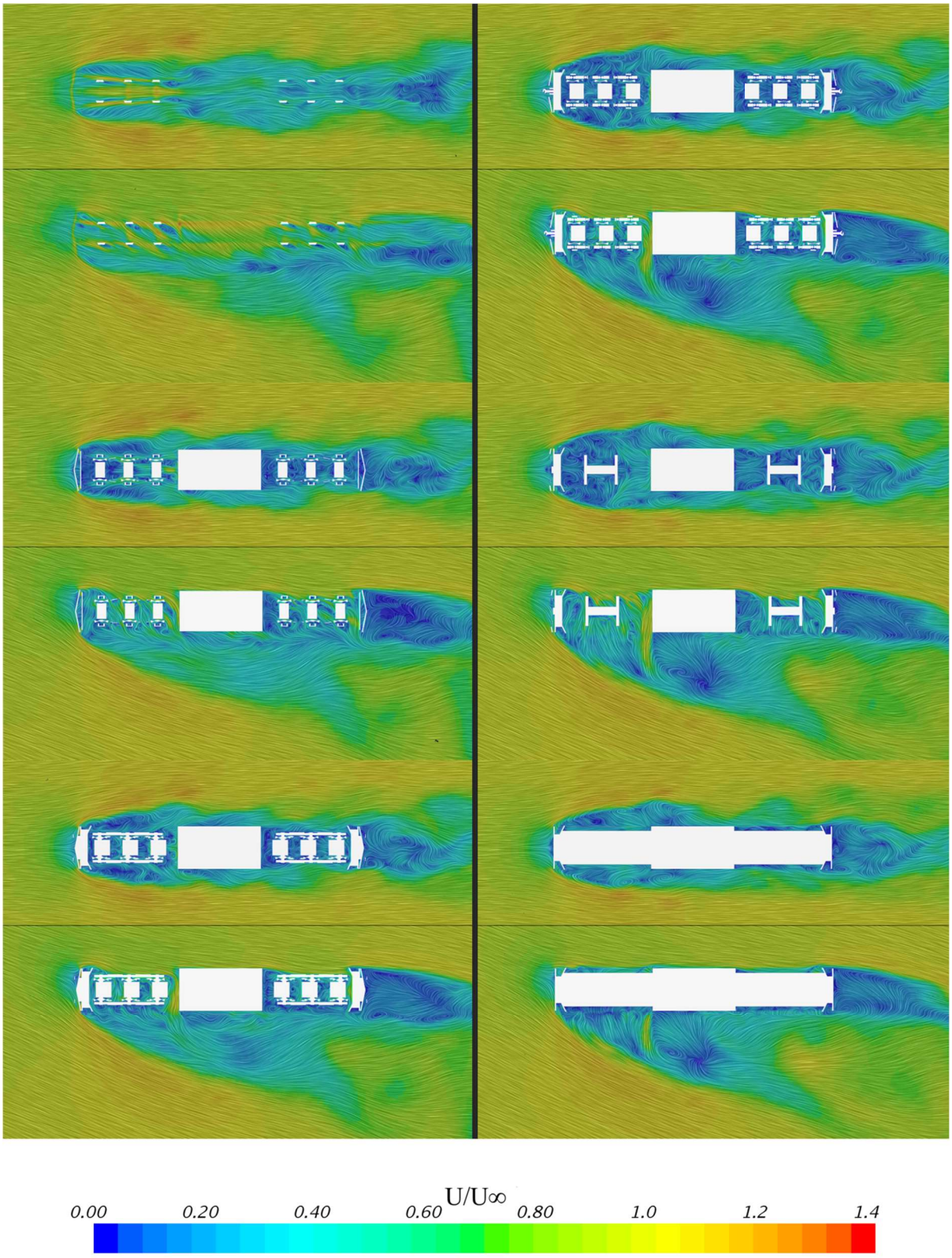

Figure 35. Plane of Streamlines Comparison of 0 Degrees and -75 Degrees. 25 cm Slices Advancing from Top to Bottom then Left to Right [.25 to 1.5 m]

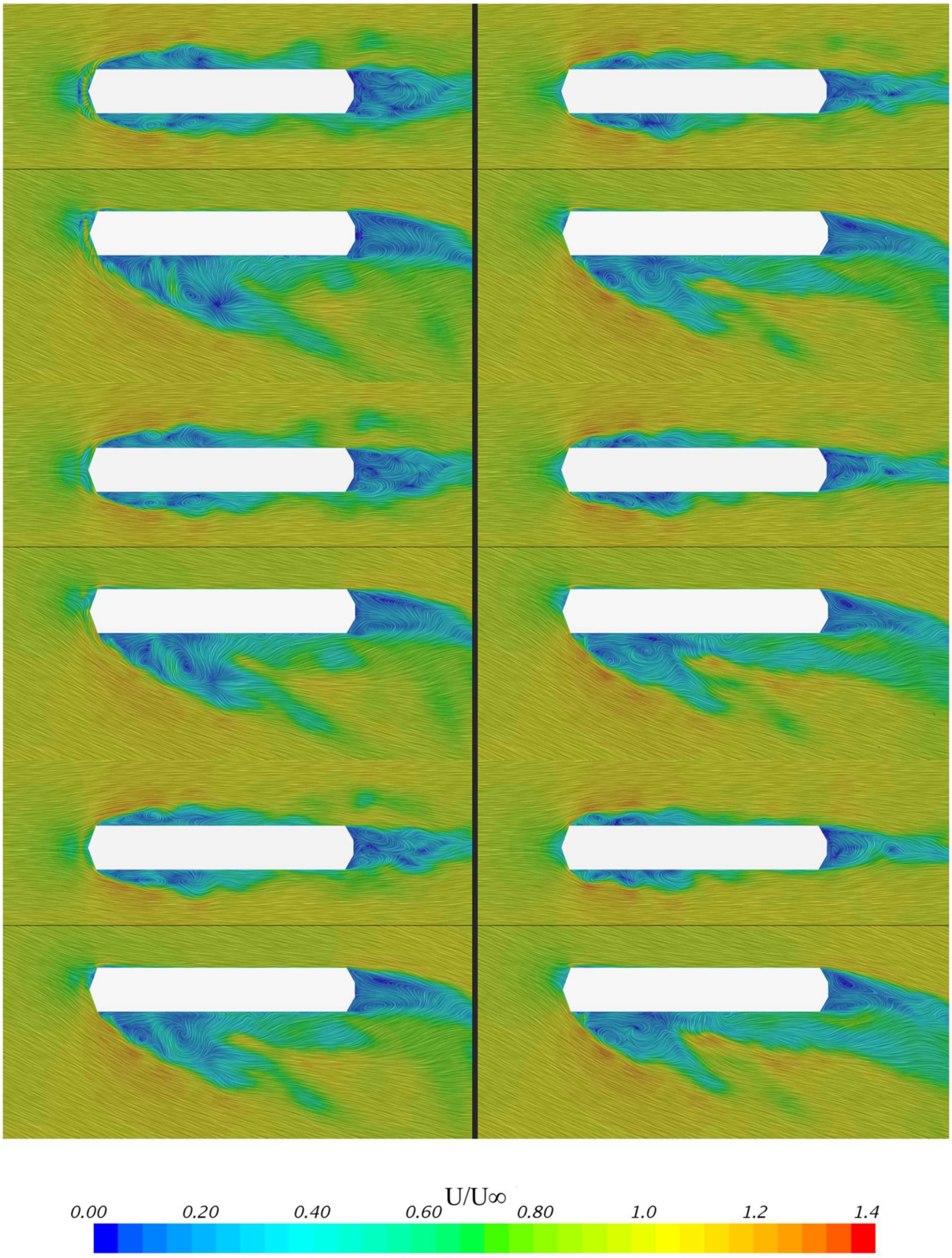

Figure 36. Plane of Streamlines Comparison of 0 Degrees and -75 Degrees. 25 cm Slices Advancing from Top to Bottom then Left to Right [1.75 to 3.0 m]

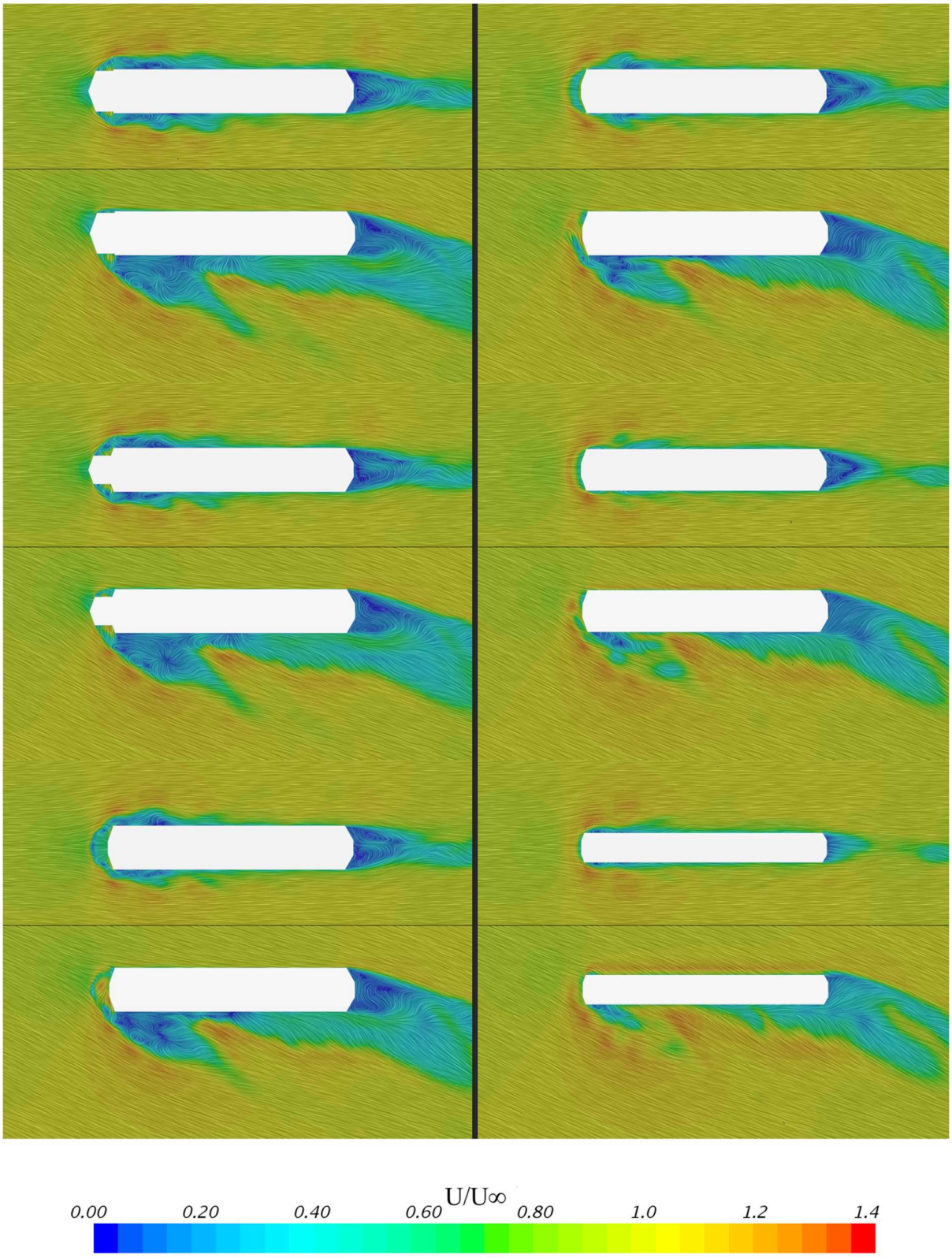

Figure 37. Plane of Streamlines Comparison of 0 Degrees and -75 Degrees. 25 cm Slices Advancing from Top to Bottom then Left to Right [3.25 to 4.5 m]

CHAPTER 5. CONCLUSION

The simulation was done using a typical freight locomotive with moving ground planes and rotating wheels with a detail set of bogies. Utilizing unsteady CFD to investigate lift, drag, and side force coefficients, a breakdown of the drag coefficient into components, and an examination of the vortical structure near by a typical freight locomotive.

The drag coefficient versus crosswind angle was compared to the Davis Peters equation and showed a general agreement. The front of the locomotive contributes the most to the drag of the locomotive followed by the rear of the locomotive. The portion of the drag coefficient from the front decreased as crosswind angle increased, but still is always the largest component. If improvements were to be made to a locomotive the front would be the easiest place to make changes from an aerodynamics standpoint. Removing the vortices from front is the easiest problem to solve. The simplest solution would be to add a cowling to the front of the train to make it more aerodynamically efficient. The vortex will still be on the leeward side of the train but will be smaller in size. If modifications to the side vortex are desired a complete change in the shape of the locomotive would be necessary to accommodate a different cross-sectional shape such as an ellipse or at least a shape with significant curvature to the sides.

The back of the locomotive contributes the second most to the drag. The scenario where there is no car behind the locomotive is the worst-case scenario for the drag coefficient. If there were a car behind the locomotive it would help close the wake region and decrease its size. This would lead to a lower drag amount on the rear face. Bogies contribute very little to the overall drag to be reduced. Simplified bogies would be useful in simulations if only the total drag is wanted. If an understanding of all the flow structures near the locomotive are wanted simplified bogies would not be enough.

A summary of observations on the flow phenomena are given below:

- The vortices coming from the front of the locomotive propagate to the leeward side of the train. The large vortical structure on the leeward side is from the separation of the flow from the large turning angle at the edge of the top of the locomotive.
- When the flow is parallel to the tracks, there are two regions of flow separation at the top of the locomotive. When there is crosswind only one smaller region of flow separation appears.
- The flow near the undercarriage and boogies is highly vortical. There is a large quantity of small scale flow structures in the boogies which would lead to a higher drag count in the region but this contribution is dwarfed by the contribution from the front and back of the locomotive.
- The vortex structure on the leeward side has a temporal component. The vortex would whip up and down and left to right over time in the simulations.
- The vortical structure on the leeward side is a combination of the three vortices from the front of the locomotive, the vortices coming from the undercarriage and boogies and, the flow separation over the top of the locomotive.

A summary of observations on the numerical data are given below:

- The individual contributions from the components of the train vary the coefficient of drag with crosswind angle.
- The ratio of the base coefficient of drag to the total coefficient drag increases while the ratio of front coefficient of drag to total coefficient of drag decreases.
- The front of the locomotive is contributing the most the coefficient of drag at each crosswind angle.

- When plotting the drag coefficients verses crosswind angle and verses wind direction angle the trends appear differently.
- When the crosswind angle is used, velocity is no longer a function of a single variable, i.e. fails the vertical line test
- When the wind direction angle is used velocity is only a function of the wind direction angle and W/T Ratio.
- When the wind direction angle is used, the components of coefficient of drag appear to be smoother on the plot than when the crosswind angle is used. This could be because the flow at wind direction angles near 90 degrees has a larger component of velocity perpendicular to the tracks. This information is lost when just using the crosswind angle as evident of the spikes in the data.

Future studies examining the W/T Ratio and seeing if the data set will collapse if used as a parameter. By playing with the W/T Ratio crosswind angles of greater than 30 degrees can be addressed. If a matrix with all W/T Ratios and Wind angles can be determined from a few CFD or wind tunnel tests, this would allow for more accurate predictions of the drag throughout the life cycle of the vehicle and potentially be used to reduce the amount of fuel used which would reduce operating costs.

The formulation of crosswind presented in this work does allow for the addition of an atmospheric boundary layer model (ABL). This would allow the addition of gust wind and the randomization of the direction of the wind. These would lead to a more accurate drag measurement between the CFD and real world.

To improve the flow modeling, switching the simulations to large eddy simulation or delayed detached eddy simulation would be preferred. This will however, require additional computational resources.

REFERENCES

Asress, Mulugeta Biadgo, and Jelena Svorcan. 2014. "Numerical Investigation on the Aerodynamic Characteristics of High-Speed Train under Turbulent Crosswind." *Journal of Modern Transportation*. doi:10.1007/s40534-014-0058-7.

Baker, C. J. 2014. "A Review of Train Aerodynamics Part 1 – Fundamentals." *The Aeronautical Journal* 118 (1201): 201–28. doi:10.1017/S000192400000909X.

CD-adapco. 2016. *STAR-CCM+® Documentation*. Version 11.04.

Committee, Truck And Bus Aerodynamics And Fuel Economy. 2013. "Guidelines for Aerodynamic Assessment of Medium and Heavy Commercial Ground Vehicles Using Computational Fluid Dynamics." SAE International.

Flynn, Dominic, Hassan Hemida, David Soper, and Chris Baker. 2014. "Detached-Eddy Simulation of the Slipstream of an Operational Freight Train." *Journal of Wind Engineering and Industrial Aerodynamics*. doi:10.1016/j.jweia.2014.06.016.

Hemida, Hassan, and Chris Baker. 2010. "Large-Eddy Simulation of the Flow around a Freight Wagon Subjected to a Crosswind." *Computers and Fluids*. doi:10.1016/j.compfluid.2010.06.026.

Menter, Florian R. 1994. "Two-Equation Eddy-Eiscosity Turbulence Models for Engineering Applications." *AIAA Journal* 32 (8): 1598–1605. doi:10.2514/3.12149.

Östh, Jan, and Siniša Krajnović. 2014. "A Study of the Aerodynamics of a Generic Container Freight Wagon Using Large-Eddy Simulation." *Journal of Fluids and Structures*. doi:10.1016/j.jfluidstructs.2013.09.017.

Peters, Jean-Luc. 1990. “Bestimmung Des Aerodynamischen Widerstandes Des ICE/V Im Tunnel Und Auf Freier Strecke Durch Auslaufversuch.” *Eisenbahntechnische Rundschau* 39: 559–64.

Rochard, B P, and F Schmid. 2000. “A Review of Methods to Measure and Calculate Train Resistances.” *Proc Instn Mech Engrs* 214.

Silvest, Tyler. 2016. “Photo Licensed under CC By 2.0.” https://www.flickr.com/photos/kansasscanner/27429644724.

Zhang, Jie, Jing juan Li, Hong qi Tian, Guang jun Gao, and John Sheridan. 2016. “Impact of Ground and Wheel Boundary Conditions on Numerical Simulation of the High-Speed Train Aerodynamic Performance.” *Journal of Fluids and Structures*. doi:10.1016/j.jfluidstructs.2015.10.006.